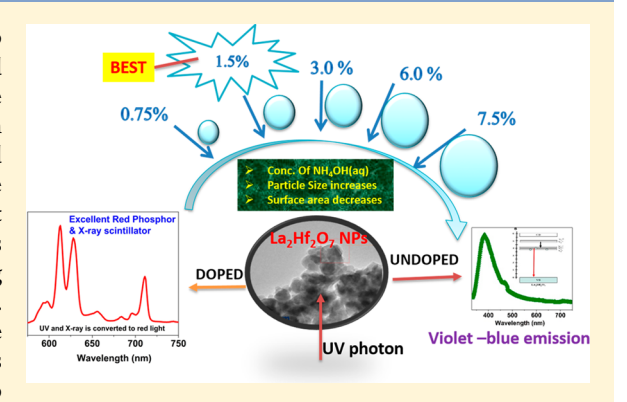
pubs.acs.org/IC

Correlating Structure and Luminescence Properties of Undoped and Eu3+-Doped La2Hf2O7 Nanoparticles Prepared with Different Coprecipitating pH Values through Experimental and Theoretical **Studies**

Santosh K. Gupta, This Jose P. Zuniga, Partha Sarathi Ghosh, Maya Abdou, and Yuanbing Mao*, Abdou, Santosh K. Gupta, This Jose P. Zuniga, Partha Sarathi Ghosh, Maya Abdou, and Yuanbing Mao*,

Supporting Information

ABSTRACT: Understanding the structure-property relationship and optimizing properties of phosphors for use in lighting and scintillation fields is an important materials challenge. In this work, we investigated the effects of the pH value of the coprecipitating solution adjusted by the concentration of NH₄OH(aq) on the structure and optical properties of the obtained La₂Hf₂O₇ nanoparticles (NPs). The obtained NPs stabilize in the ideal pyrochlore structure, but the extent of ordering increased with an increase in the pH value used. The NPs prepared at pH = 12.1 displayed the best optical performance owing to the balance of the crystallinity, agglomeration, and surface defects. On the basis of density functional theory (DFT) calculations, the origin of violet-blue emission in undoped La₂Hf₂O₇ NPs was attributed to defect states in the electronic band gap arising due to



oxygen defects. For the La₂Hf₂O₇:Eu³⁺ NPs, the Eu³⁺ dopants possess low symmetry and their occupancy is more favorable at the LaO₈ site. DFT calculations further justify the complete host-to-dopant energy transfer and origin of the most intense red emission observed experimentally. Understanding the interplay of the experimental and theoretical results thus is a very useful general approach for improving the efficiency of luminescent materials.

1. INTRODUCTION

Research pertaining to A₂B₂O₇ nanoparticles (NPs) has gained significant interest in the past decade mainly because of their diverse applications in areas of technological importance, such as magnetic materials, electrocatalysis, 2,3 host materials for nuclear waste,⁴ luminescence,⁵⁻⁷ oxygen conductors,⁸ scintillators,^{7,9} etc. Because they exhibit potential superior physical and chemical properties compared to their bulk counterparts, much effort has been envisaged to enhance their sinterability and other optical, catalytic, and magnetic properties for advanced applications in optoelectronics. Nanophosphors are more favorable to having uniform morphology, homogeneous composition, and good surface properties, which all influence their physical and chemical properties and ultimately determine their applications. 10 However, understanding their structure-property relationship and optimizing their properties is still an important materials challenge, e.g., for their use in lighting and scintillating fields.

One of the structure variables of functional materials is the type and number of defects, which lead to various interesting properties, such as light emission, 12,13 ferromagnetism, electrocatalysis, 15 etc. A₂B₂O₇-type materials are known to have an abundance of defects, which impart various interesting

properties in them, such as high radiation stability in $Gd_2Zr_2O_7$, 16 photoluminescence (PL) in $Nd_2Zr_2O_7$, 17 ionic conductivity in $Gd_2Ti_2O_7$, 18 magnetism in $Y_2Ti_2O_7$, 19 and electronic properties in $Bi_2Ru_2O_7$. As one of the most important rare-earth hafnates, $La_2Hf_2O_7$ has been envisaged for doping-induced emission, $^{5,7,9,21,22}_{,1,22}$ noncontact thermometry, $^{23}_{,2,1,2,2}$ and solid oxide fuel cells. 24 In addition, $La_2Hf_2O_7$ is envisaged to be a very good dielectric material because of its rather low defect density and less Fermi-level pinning than HfO2. Also, because of its high stopping power for X-rays and γ -rays with atomic number $Z_{\rm Hf} = 72$ and a high density of 7.9 g cm⁻³, it was found to be very attractive for novel high-energy radiation detectors. Considering the PL and radioluminescence (RL) of undoped $\text{La}_2\text{Hf}_2\text{O}_7$, Eagleman et al. observed blue emission around 460 nm in the microcrystalline sample, which was attributed to the presence of oxygen vacancies. However, there is no report of such measurement from La₂Hf₂O₇ NPs. Moreover, oxygen vacancies have three different identities: neutral, singly ionized, and doubly ionized. 14,17 Previously, no calculation has been taken to confirm the possible mechanism

Received: July 15, 2018 Published: September 4, 2018



11815

 $^{^\}dagger$ Department of Chemistry and $^\parallel$ School of Earth, Environmental, and Marine Sciences, University of Texas Rio Grande Valley, 1201 West University Drive, Edinburg, Texas 78539, United States

[‡]Radiochemistry Division and [§]Materials Science Division, Bhabha Atomic Research Centre, Trombay, Mumbai 400085, India

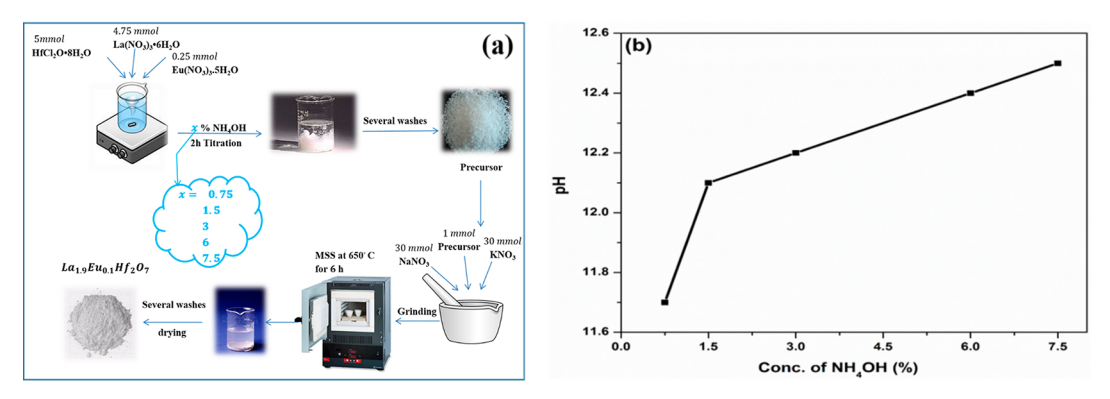


Figure 1. (a) Schematic of the combined coprecipitation and MSS procedure for the $La_2Hf_2O_7$:5% Eu^{3+} NPs using the precipitant $NH_4OH(aq)$ solution under different pH values. (b) Variation of the pH value as a function of the $NH_4OH(aq)$ concentration during the coprecipitation process.

of blue emission and the involved transitions. Also, Gu et al. synthesized $La_2Hf_2O_7$ pyrochlore samples at 550 °C using a combustion method. These samples have micron-sized grains and do not have the efficacy of NPs, which is very important for the creation of thermally and chemically resistant support for catalysts and materials for chemosensors.

Synthesis methods have great influence on the properties of materials, especially the optical performance of luminescent NPs.³⁰ The changes could be triggered by precursor selection, modification of the reaction conditions, postsynthesis processing, etc. 17,31-35 For example, an increase of the synthesis time or temperature could lower the surface defect density and luminescence quenching and so enhance the quantum yield (QY) of luminescent NPs; however, it also could induce undesirable particle growth and agglomeration, which may scatter excitation/emission light and eventually compromise the overall performance of luminescent NPs.³⁶ In recent years, our group has developed a combined coprecipitation and molten-salt synthesis (MSS) procedure to synthesize A₂B₂O₇ NPs size-controllably. The pH value of the coprecipitation step is a very important factor that governs the physical and microstructural properties of the synthesized NPs. 37-40 While our synthesis procedure has many advantages, such as simplicity, greenness, reliability, scalability, and generalizability, ^{41,42} to the best of our knowledge, no study has been reported on the systematical investigation of the influence of the pH value during the synthesis of these NPs on their structural characteristics, defect chemistry, and luminescence properties.

Therefore, in this report, we first changed the pH value of the coprecipitation solution by altering the added NH₄OH(aq) concentration during the coprecipitation process. After the consequent MSS processing of the obtained single-source complex precursor, we made La₂Hf₂O₇ NPs at relatively low temperature with well-controlled shape and size. He mission and the oxygen vacancy identity in the undoped La₂Hf₂O₇ NPs. This was done through PL spectroscopy and density functional theory (DFT) calculations based on the calculated densities of states (DOSs) for ideal, neutral, singly ionized, and doubly ionized oxygen vacancies of La₂Hf₂O₇. Moreover, the presence of oxygen vacancies was further confirmed by annealing the La₂Hf₂O₇ NPs in different atmospheres and comparing the emission profiles of the obtained samples.

To further correlate the structure and luminescence properties of the La₂Hf₂O₇ NPs, we doped them with trivalent

Eu³⁺ ions to serve as the most preferred spectroscopic probe because of its nondegenerate ground state (${}^{7}F_{0}$) and emissive state (${}^{5}D_{0}$). Europium is known as an efficient red-emitting ion doped in various kinds of inorganic phosphors such as zirconate, aluminate, tungstate, vanadate, etc. ${}^{43-46}$

Doping NPs is an efficient way of tailoring various properties of materials such as catalytic, magnetic, optical, etc., properties. However, sometimes in a system with multiple doping sites such as La₂Hf₂O₇, it becomes imperative to know the actual local structure of the dopant. It is also imperative to design materials with high catalytic activity, high light emission efficiency, and efficient magnetic properties. For the Eu³⁺doped La₂Hf₂O₇ NPs, here we explained the low-symmetric environment of Eu3+ ions in the La2Hf2O7 host by virtue of DFT-calculated cohesive energies. The luminescence in doped samples is governed by the energy-transfer process (ETP) from the host to the dopant ion. Understanding the dynamics of ETP in doped phosphors sometimes becomes very imperative in the design of a tunable phosphor. In that direction, in this work, we used DFT to calculate the DOS for the Eu³⁺-doped La₂Hf₂O₇ NPs and proposed the mechanism for energy transfer in them. We found that there is a close correlation between the experimental and theoretical results.

Therefore, this is indeed the only report of its kind wherein the experimental and theoretical evidence for defect-induced emission in undoped $La_2Hf_2O_7$ NPs and the local structure and host-to-dopant energy transfer in its doped counterpart are investigated. Such studies are unprecedented in the design of highly efficient phosphors for light-emitting diodes (LEDs) and scintillators. A novel approach of making different-sized NPs by changing the pH during coprecipitation and its effect on the QY, PL, RL, and emission kinetics of both undoped $La_2Hf_2O_7$ and $La_2Hf_2O_7$: Eu^{3+} NPs has also been demonstrated. Together with these studies, the thermal stability is also evaluated for the Eu^{3+} -doped $La_2Hf_2O_7$ NPs, which are important for applications as field-emission displays and plasma display panels.

2. EXPERIMENTAL SECTION

2.1. Synthesis of La₂Hf₂O₇ and La₂Hf₂O₇:Eu³⁺ NPs. In this study, we synthesized undoped and 5.0% Eu^{3+} -doped La_2 Hf₂O₇ NPs using a combined coprecipitation and MSS method, as reported in our earlier work (Figure 1a). 5,9,22,41,42 The starting materials were all analytical-grade reagents, including lanthanum nitrate hexahydrate $[La(NO_3)_3 \cdot 6H_2O, 99.0\%]$, hafnium dichloride oxide octahydrate (HfOCl₂·8H₂O, 99.0%), and europium(III) nitrate pentahydrate $[Eu(NO_3)_3 \cdot 5H_2O, 99.9\%]$, and were used without further purifica-

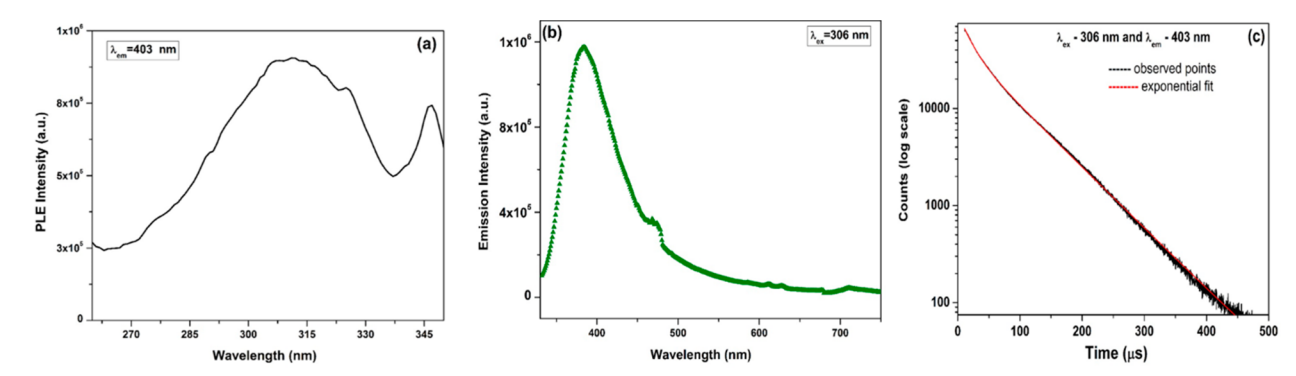


Figure 2. (a) Excitation spectrum at λ_{em} = 403 nm. (b) Emission spectrum at λ_{ex} = 306 nm. (c) PL decay profile of the La₂Hf₂O₇ NPs (LHO-S0.75).

tion. In a typical synthesis, they were first measured in a stoichiometric ratio and dissolved in 200 mL of water (Millipore, 18.2 M Ω at 25 °C). An ammonium hydroxide aqueous solution with different concentrations (0.75-7.5%) was used for coprecipitating out the metal ions and resulted in different pH values of the precipitating solution (Figure 1b). The pH of the precipitating solution after ammonium hydroxide addition was measured using a potable pH meter. This first step allowed for the formation of a single-source precursor of La(OH)3·HfO(OH)2·nH2O or % La(OH)3·5% Eu- $(OH)_3 \cdot HfO(OH)_2 \cdot nH_2O$ corresponding to the undoped or 5% Eu³⁺ doped La₂Hf₂O₇ NPs via the coprecipitation process. In the next MSS step, potassium nitrate (KNO₃, 99.9%), sodium nitrate (NaNO₃, 98%), and the formed single-source precursor were mixed in a weight ratio of 30:30:1 and ground together into a fine powder. Then the resulting mixture was transferred into a corundum crucible and placed in a muffle furnace. The furnace was set to run at 650 °C for 6 h with ramp-up and -down rates of 10 °C min⁻¹. The synthesized La₂Hf₂O₇ and La₂Hf₂O₇:5% Eu³⁺ NPs were washed multiple times with deionized water to deionize any residual salt from the surface of the NPs. The MSS method was utilized because it allows for the formation of size-controlled NPs at relatively low temperature of these refractory metal oxides while ensuring no phase transformation. Their particle size was tuned by changing the pH value of the coprecipitation solution using different concentrations of NH₄OH-(aq) solution. Correspondingly, on the basis of the concentration of the NH₄OH(aq) solution used, the undoped La₂Hf₂O₇ NPs were labeled as LHO-S0.75, LHO-S1.5, LHO-S3, LHO-S6, and LHO-S7.5, respectively, and the La₂Hf₂O₇:5% Eu³⁺ NPs were labeled as LHOE-S0.75, LHOE-S1.5, LHOE-S3, LHOE-S6, and LHOE-S7.5, respectively.

2.2. Theoretical Methodology. The methodologies adopted for hybrid functional DFT (HSE06) calculations and defect formation energy calculations are described in the Supporting Information.

3. RESULTS AND DISCUSSION

3.1. Phase Purity, Surface Area, and Morphology: X-ray Diffraction (XRD), Brunauer–Emmett–Teller (BET), and Electron Microscopy. The phase purity of the LHO and LHOE NPs has been characterized by powder XRD, and the obtained pattern is shown in Figure S1, with the calculated crystallite sizes listed in Table S1. The Rietveld-refined XRD profile was carried out on the representative La₂Hf₂O₇:Eu³⁺ NPs (LHOE-S3) and is shown in Figure S2.

The N_2 adsorption isotherms and corresponding fittings for the $La_2Hf_2O_7$ NPs are shown in Figure S3.⁴⁷ The morphology and relevant changes of the NPs are shown in Figures S4–S6 along with a discussion.

3.2. Structural Analysis: Fourier Transform Infrared (FTIR) and Raman Spectroscopy. On the basis of the XRD patterns (Figure S1), it is very difficult to distinguish between

an ordered pyrochlore (OP) phase and a disordered fluorite (DF) structure when the structure factors are comparable to those in Gd₂Zr₂O₇. ⁴⁸ The OP structure can be described as a superstructure of fluorite (the lattice parameter of OP is twice that of DF). In general, the XRD patterns of the OP phases contain very weak superlattice peaks that could hardly be seen in the fluorite phases. The superlattice reflections (when the pyrochlore is viewed as a derivative of fluorite) are the (111), (331), and (531) reflections due to both cations. If the structure factors of the two cations are comparable, the intensities of the superlattice reflections arise mostly because of scattering of the anions. In such a case, if the anion lattice is made up completely of oxygen atoms, the XRD patterns give very weak ordering reflections. Luckily, Raman and FTIR spectroscopy techniques can be used to distinguish between the DF and OP structures.

Because the bending and stretching of the metal—oxygen (M–O) bond in the pyrochlore lattice is IR-active, FTIR spectroscopy has been extensively used to investigate the nature of the M–O bonds in the $A_2B_2O_7$ pyrochlore compounds. Subramanian and his group in one of their classical works on the structure of pyrochlore reported that the IR spectra of $A_2B_2O_7$ oxides consist of seven IR modes in the range of 750–50 cm⁻¹, arising due to the bending and vibration of the M–O bonds. As shown in the FTIR spectra of the $A_2H_2O_7$ NPs (Figure S7), the IR band around 610 cm⁻¹ (ν_3) is attributed to the Hf–O stretching in the HfO6 octahedra and the one at ~426 cm⁻¹ (ν_1) to the La–O stretching in the A_2O_8 scalenohedra. The peak at 521 cm⁻¹ (ν_2) corresponds to the A_2O_8 scalenohedra. Thus, FTIR spectra further confirmed the presence of A_2O_8 and A_2O_8 moieties, and these vibrations confirmed the formation of the A_2O_7 structure.

Figure S8 shows the Raman spectra of the undoped and ${\rm Eu^{3+}}$ -doped ${\rm La_2Hf_2O_7}$ NPs prepared from the coprecipitation of solutions with various pH values, similar to those reported in the literature. There is not much change in the Raman spectra of the undoped and doped ${\rm La_2Hf_2O_7}$ NPs, indicating that the basic pyrochlore network remains intact and is stable even on a doping europium ion. However, local disorder can occur in the pyrochlore structure. It often results in an increase in the peak broadening (full width half-maximum, fwhm) of Raman bands. It can be seen that at the highest pH value used in the coprecipitating solution the fwhm of Raman band is very narrow compared to the lowest pH value. This indicates that the extent of ordering increases as the pH is raised, and at lower pH, the ${\rm La_2Hf_2O_7}$ NPs still have some lattice

m 11 1	CCA LIDA	C 1 1 4 1 F 111 1	T 441 D	A D	D 17 41 15	0 1 0
Lable I.	. CTCTA- and LIDA-	Calculated Equilibrium	n Lattice Parameters.	Atomic Positions.	Bond Lengths, and	Band Gabs

$La_2Hf_2O_7$	a_0 (Å)	x	$La-O_{8b}$ (Å)	$La-O_{48f}$ (Å)	$Hf-O_{48f}$ (Å)	band gap (eV)
GGA	10.806	0.330	2.34	2.65	2.10	4.18
LDA	10.603	0.331	2.30	2.59	2.06	4.15
HSE06						5.63
experiment	10.776 ⁵⁶		2.333^{56}	2.555^{56}	2.090^{56}	5.6 ± 0.1^{58}
	10.750 ⁵⁷			2.554 ⁵⁷	2.150 ⁵⁷	

disordering. This can also be seen from the highest intensity of the breathing mode from the samples prepared with the lowest pH and the minimal intensity from those made from the highest pH used. At lower pH, it is possible that there is relatively more disruption of the translational symmetry, which allows more phonons to contribute to the optical spectra, resulting in peak broadening. ⁵³

3.3. PL Studies. 3.3.1. PL Properties of the $La_2Hf_2O_7$ NPs. Figure 2a displays the excitation spectrum of the undoped La₂Hf₂O₇ pyrochlore NPs (S0.75) at an emission wavelength of 403 nm. The excitation spectrum displayed a broad band peaking at around 306 nm that is attributed to $\mathrm{O^{2-}} \rightarrow \mathrm{Hf^{4+}}$ charge transfer. The emission spectrum recorded with 306 nm excitation showed a peak around 403 nm in the violet-blue region, as shown in Figure 2b. It is very interesting to see the visible color emission in the La₂Hf₂O₇ NPs under irradiation with 306 nm light. Such PL in the NPs without any activator or dopant ion is a significant development in the field of dopantfree luminescent materials. It is very difficult to find a suitable violet-blue phosphor for two reasons: (a) it needs a wide-bandgap host; (b) our naked eyes have very low sensitivity in the violet-blue spectral region. Such visible emission in a nanomaterial without any dopant ion can be ascribed to defect state(s) in the band gap of the material. On the basis of the synthesis technique, annealing temperature, crystal structure, pH conditions, etc., the NPs can have abundant structural defects such as the cation vacancy, cation antisite, oxygen vacancy, oxygen antisite, cation interstitial, and oxygen interstitial.⁵⁴ Moreover, depending on the number of electrons a material has trapped, there are different kinds of oxygen vacancies, namely, neutral (F center), singly ionized (F+ center), and doubly ionized $(F^{2+}$ center) corresponding to 0, 1, and 2 electrons trapped. To exactly identify the defect responsible for the violet-blue emission in the La₂Hf₂O₇ pyrochlore NPs, luminescence decay profiles were recorded and are shown in Figure 2c. The PL decay curve was fitted using a monoexponetial model with a lifetime value of 9.62 μ s.

The emission at 403 nm (violet-blue) cannot be attributed to any kind of exciton emission because of the large band gap of La₂Hf₂O₇. However, it is in close resemblance with the F⁺ center emission of HfO₂. Its lifetime value ($\tau = 9.62~\mu s$) also indicates that it is due to the presence of a singly ionized oxygen vacancy (V_O¹⁺) or the F⁺ center involving the ²T_{1u} \rightarrow ²A_{1g} transitions of the F⁺ center around the octahedral hafnium atom.

Such visible emission was also observed previously in a rareearth zirconate pyrochlore. It was attributed to the presence of oxygen vacancies in the band gap of the host material. ^{17,54,55} It is known that in the La₂Hf₂O₇ structure there exist two different kinds of oxygen vacancies with T_d (O_a) and $C_{2\nu}$ (O_b) symmetries. O_a is surrounded by four La³⁺ ions, whereas O_b is surrounded by two La³⁺ and two Hf⁴⁺ions. It is expected that our La₂Hf₂O₇ NPs emit violet-blue light under UV irradiation because of the presence of some defects, most probably oxygen

vacancies. Therefore, we used DFT to calculate the DOS of the ${\rm La_2Hf_2O_7}$ NPs to investigate their oxygen-vacancy-induced electronic states.

In the pyrochlore La₂Hf₂O₇ NPs, the lanthanum and hafnium atoms are located at $(16d)^{1}/_{2}$, $^{1}/_{2}$, $^{1}/_{2}$ and (16c) 0, 0, 0 sites, respectively, and the cations alternate on the facecentered-cubic sublattice in rows along the (110) directions. The anion sublattice is comprised of three different oxygen sites, two of which are occupied, (8b) $^{3}/_{8}$, $^{3}/_{8}$, and (48f) x, $^{1}/_{8}$, $^{1}/_{8}$, and the third, (8a) $^{1}/_{8}$, $^{1}/_{8}$, of which is vacant. Table 1 shows our DFT-calculated equilibrium lattice parameters, internal parameters, bond lengths, and band gaps using the local density approximation (LDA) and generalized gradient approximation (GGA). As can be seen from the table, the calculated lattice parameters match well with the experimental values (with <1.5% difference) and GGA is predicting the closest value to the experimental lattice parameters. Both LDA- and GGA-calculated internal parameters (x) and bond lengths match well within 5% of the experimental values.

Our PL study and also the investigation by Eagleman and his group²⁶ show that emission in LHO is due to the presence of oxygen vacancies. Therefore, we calculated the electronic DOS of an ideal LHO and changes in the electronic DOS in the presence of oxygen vacancies (neutral and charged). To generate oxygen vacancy defect structures, one oxygen atom is removed from the ideal LHO unit cell of 88 atoms. The total energy of the ideal LHO unit cell (containing 88 atoms) and structures comprised of oxygen vacancies (neutral and charged) were optimized with respect to the volume (or lattice parameter) and atomic positions. Figure 3A(a) presents the total- and orbital-angular-momentum-resolved DOSs for LHO, where the Fermi level is set to 0 eV. The valence bands (VBs) are mainly contributed by O 2p orbitals hybridized with Hf 5d orbitals. The conduction band (CB) is mainly composed of La 4f states and antibonding states of Hf 5d. Our HSE06calculated electronic band gap of 5.63 eV demonstrates the insulating character of LHO. By using the photoconductivity spectrum, Seguini et al.⁵⁹ demonstrated that the band gap of $La_2Hf_2O_7$ is 5.6 \pm 0.1 eV in the amorphous phase. Our HSE06-calculated band gap is in excellent agreement with the experimental value. Moreover, Terki et al.⁶⁰ used the DFT +LAPW method implemented in WIEN2K codes to examine the DOS of La₂Hf₂O₇ and reported a 3.34 eV direct band gap, which is underestimated compared to the experimental result and our value obtained from LDA/GGA calculations.

Figure 3A(b) presents the total- and angular-momentum-decomposed DOS due to the presence of a neutral oxygen vacancy (V_O^0) . The spin-up and spin-down components are shown separately in the upper and lower panels, respectively. While the overall nature of the VB remains unaltered, a doubly occupied impurity band appears 3.5 eV ahead of the VB maximum in the band gap and below the Fermi level. This impurity band is mainly contributed by the La d/f and O p

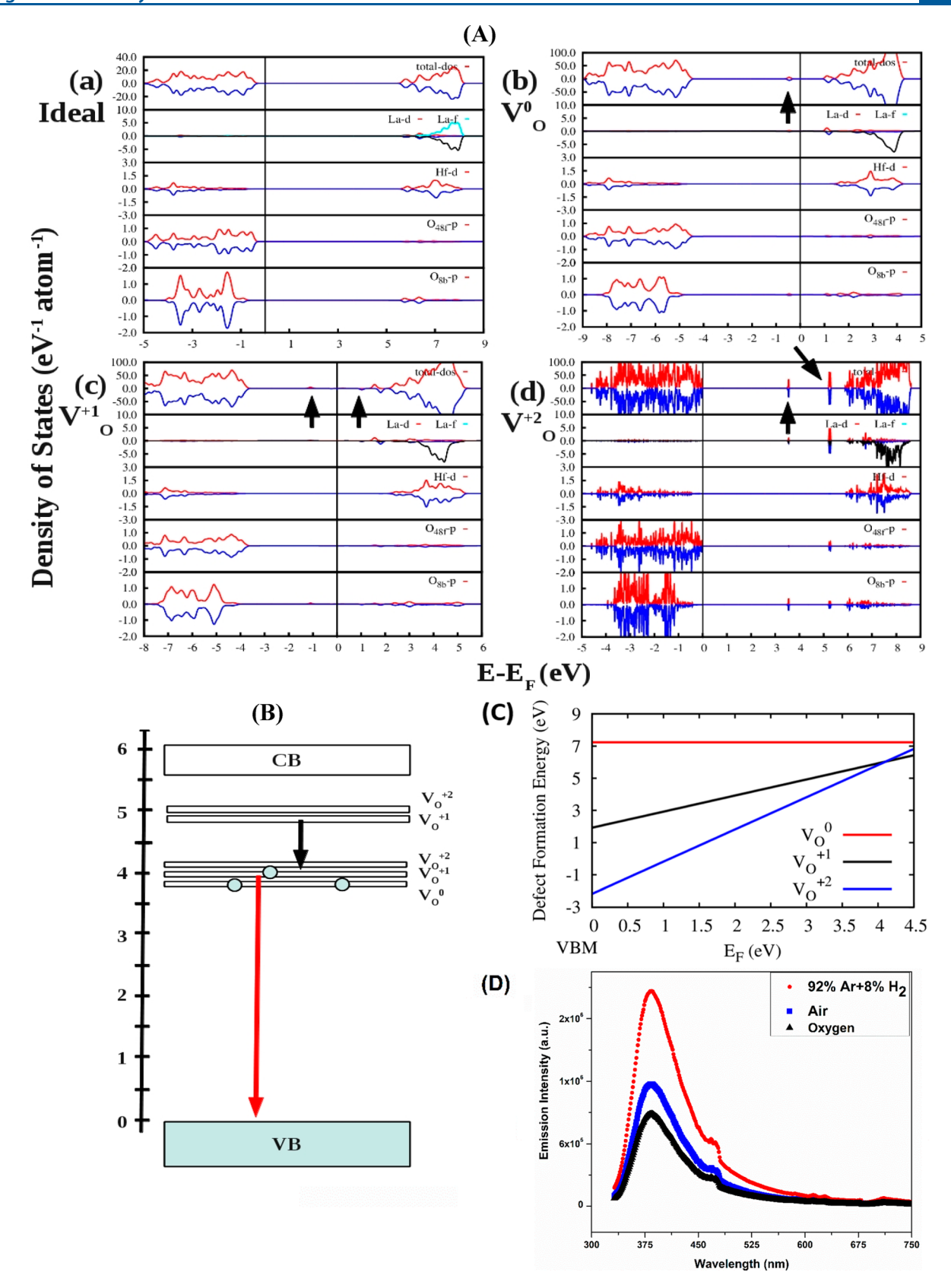


Figure 3. (A) HSE06-calculated total- and angular-momentum-decomposed DOSs of (a) the ideal pyrochlore $La_2Hf_2O_7$, (b) a pyrochlore with a neutral oxygen vacancy (V_O^{1}) , (c) a pyrochlore with an oxygen vacancy of charge $1+(V_O^{1+})$, and (d) a pyrochlore with an oxygen vacancy of charge $2+(V_O^{2+})$. Defect states are marked by arrows. Vertical lines at 0 eV present the Fermi energy. (B) Location of the defect states (calculated using DFT–HSE06) in the electronic band gap of $La_2Hf_2O_7$ in neutral and charged defect states. (C) Formation energies of oxygen vacancies in bulk $La_2Hf_2O_7$, in the dilute limit, calculated with DFT–HSE06 as a function of the Fermi energy, in the oxygen-rich limit. (D) Emission spectra ($\lambda_{ex} = 306$ nm) of the as-synthesized LHO-S0.75 NPs and those after annealing in oxygen and 92% Ar + 8% H₂.

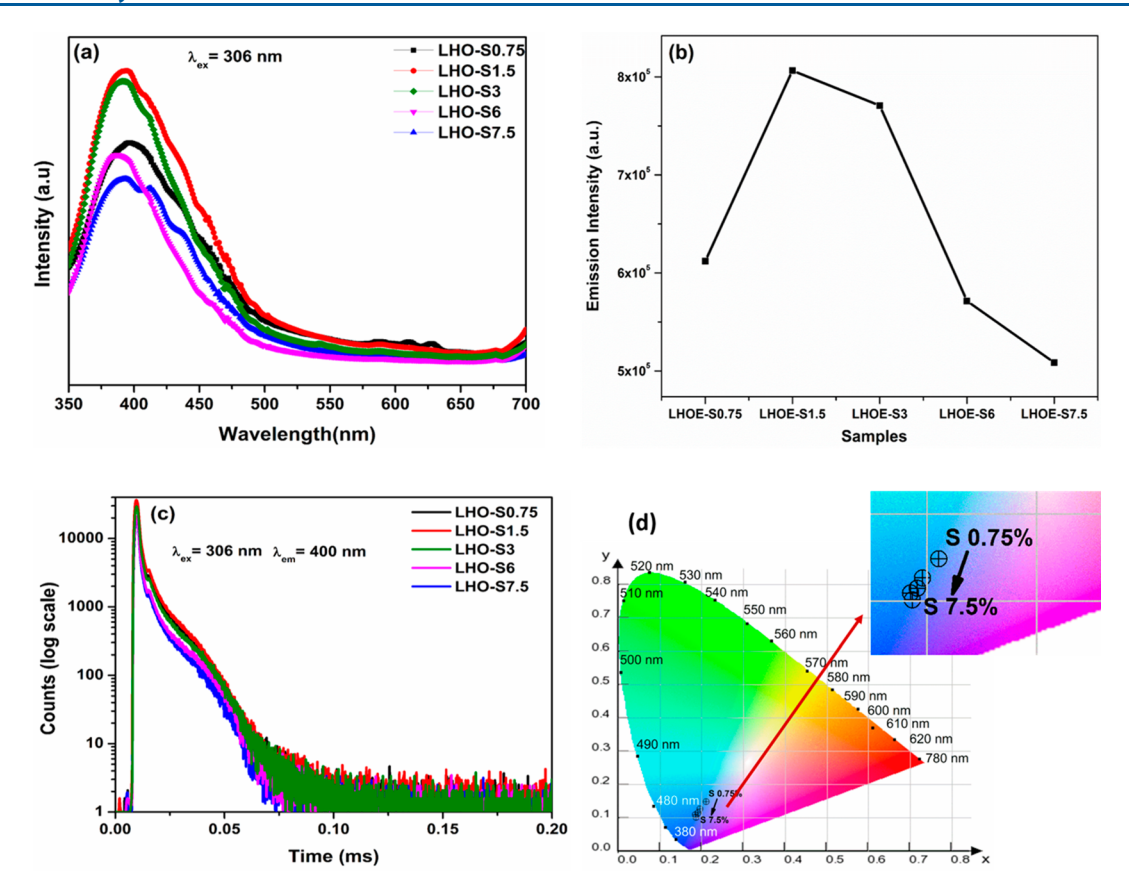


Figure 4. (a) Emission spectra taken at $\lambda_{\rm ex} = 306$ nm. (b) Corresponding emission intensity variation with the different [NH₄OH] used. (c) PL decay profiles taken at $\lambda_{\rm ex} = 306$ nm and $\lambda_{\rm em} = 396$ nm. (d) CIE color coordinate diagram of the La₂Hf₂O₇ NPs coprecipitated at various pH values. The inset of part d shows the magnified CIE coordinates of the LHO NPs.

states. For this case $(V_O^{\ 0})$, the energy difference between the VB maximum and CB minimum (electronic band gap) is 5.1 eV.

Figure 3A(c) presents the total- and angular-momentum-decomposed DOS due to the presence of an oxygen vacancy with charge $1+({\rm V_O}^{1+}).{\rm V_O}^0$ becomes ${\rm V_O}^{1+}$ by trapping a hole from its surroundings. The overall nature of the VB remains unaltered, but doubly occupied impurity states split up into two impurity states. Impurity states generated by spin-up components are filled with electrons because they are situated below the Fermi energy. Impurity states generated by spin-down components are empty. The impurity levels are composed of La d/f and O p states. The filled defect states are present 2.1 eV ahead of the VB, and the energy difference between the VB maximum and CB minimum (electronic band gap) for the ${\rm V_O}^{1+}$ case is 4.7 eV.

Figure 3A(d) presents the total- and angular-momentum-decomposed DOS due to the presence of an oxygen vacancy with charge 2+ $({\rm V_O}^{2+})$. The overall nature of the VB remains unaltered, but an impurity band appears above the VB maximum in the band gap. The Fermi level is situated just above the VB maximum. Impurity bands are present 3.5 and 5.2 eV ahead of the VB maximum. The impurity levels are composed of La d and O p states in both the spin-up and spin-down components. For this case, the energy difference between the VB maximum and CB minimum (electronic band gap) is 5.6 eV.

Figure 3B shows a complete summary of the locations of the defect states in the band-gap region, as calculated from our DFT-HSE06. The emission spectrum of the LHO sample

shows a broad emission peak around the 400 nm region (Figure 2b). This broad peak corresponds to optical emission between states that are situated 3.60-2.75 eV away from each other. In La₂Hf₂O₇, the defect states near 4.0 eV consist of V_0^0 , ${
m V_O}^{1+}$, and ${
m V_O}^{2+}$. Among them, the ${
m V_O}^0$ states are filled with electrons (shown by two circles) and the ${
m V_O}^{1+}$ state is partially filled (shown by one circle). The other states are empty. Violet-blue emission can be explained as the transition of an electron from the defect state to the VB. In LHO, there are no defect states near the CB, but defect states are present almost 0.6 eV away from the CB. The transition from those states to other defect states (which are present almost 1.0 eV below) gives emission that could not fall in the visible region. Moreover, in the previous paragraph, it is shown that the generation of V_O^{0} and V_O^{1+} defects reduces the electronic band gap of LHO. Therefore, our DFT-HSE06 results qualitatively provide an explanation for the origin of a broad emission peak in our undoped LHO NPs.

Figure 3C shows DFT–GGA-calculated defect formation energies in the dilute limit for neutral $(V_O^{\ 0})$ and charged $(V_O^{\ 1+}$ and $V_O^{\ 2+})$ oxygen defects. The formulas to calculate the defect formation energies are described in our previous study, ¹⁷ and an experimental dielectric constant of 25^{61} is employed in these calculations. The calculated vacancy formation energy values indicate that the formation of $V_O^{\ 2+}$ defects is most favored near the VB compared to $V_O^{\ 1+}$ and neutral oxygen defects, indicating that the oxygen vacancies have a tendency to donate electrons or behave as an n-type defect. The formation of a neutral oxygen vacancy is energetically less favorable compared to charged oxygen defects, and vacancy

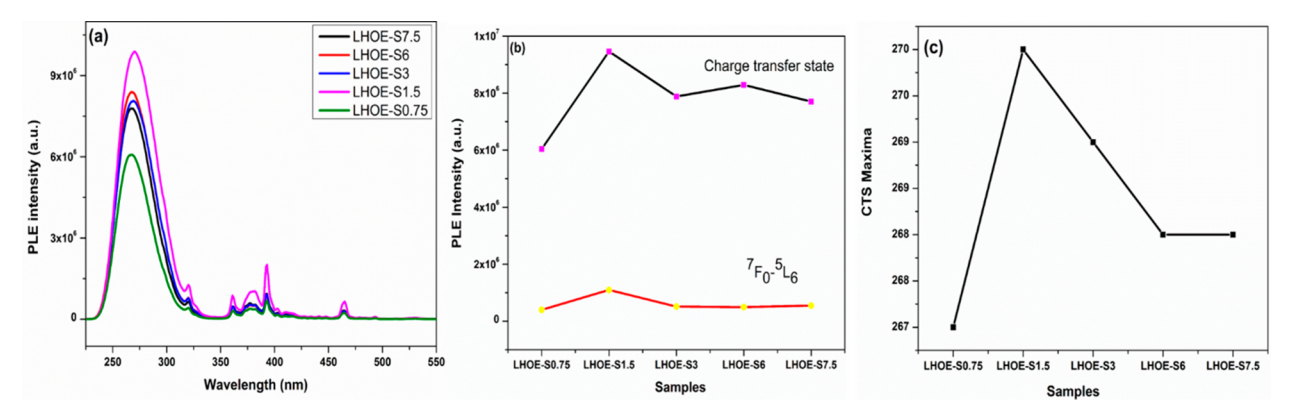


Figure 5. (a) Excitation spectra, (b) variation of the PLE intensity, and (c) variation of the CTB maxima as a function of the coprecipitating pH of the LHOE NPs.

formation energies of 1+ and 2+ oxygen defects become close by with increasing Fermi energy. The vacancy formation energy of $V_{\rm O}{}^0$ is high compared to charged defects, and $V_{\rm O}{}^0$ defect states are fully occupied [Figure 3A(b)]. On the contrary, $V_{\rm O}{}^{1+}$ and $V_{\rm O}{}^{2+}$ defect states are partially filled [Figure 3A(c)] and empty [Figure 3A(d)], respectively. Therefore, the defect states (arising due to $V_{\rm O}{}^{1+}$ and $V_{\rm O}{}^{2+}$ defects) are expected to participate strongly in the PL emission of the LHO NPs.

To confirm that it is indeed oxygen vacancies that are responsible for violet-blue emission in our La₂Hf₂O₇ NPs, we annealed our as-synthesized NPs at 650 °C for 6 h in pure O2 and a reducing atmosphere (8% H₂ + 92% Ar) and compared their emission spectra with that of the as-synthesized sample in air (Figure 3D). To rule out the formation of any unwanted phase after annealing in oxidizing pure O2, air, and a reducing atmosphere (8% H₂ + 92% Ar), XRD data and Raman spectroscopy were taken from the annealed La₂Hf₂O₇ NPs (Figure S9). The XRD patterns and Raman spectra did not reveal the formation of any other phases, and they are stabilized as La₂Hf₂O₇ pyrochlore NPs. It is very interesting to see that the intensity of violet-blue emission reduces for the NPs annealed in pure O2, whereas it increases for the NPs annealed in a reducing H2 atmosphere compared to the original NPs. Pure O2 presents a completely oxidizing environment, which combines with oxygen vacancies presented in the as-synthesized La₂Hf₂O₇ NPs. Therefore, the oxygen vacancy defect density reduces, and correspondingly the PL intensity decreases. On the other hand, the defect density is increased after annealing in a reducing atmosphere, which creates more oxygen vacancies compared to the as-synthesized sample (in air). Similar justification has been given to calcium zirconate NPs to explain its blue emission. 62 These results indicate that PL presented in the violet-blue region from our as-synthesized La₂Hf₂O₇ NPs is invariably due to the oxygen vacancies acting as radiative centers.

3.3.2. Effect of the Coprecipitating pH on the PL Properties of the $La_2Hf_2O_7$ NPs. Figure 4a shows the emission spectra of the $La_2Hf_2O_7$ NPs after excitation at 306 nm. It can be seen from Figure 4b that the emission intensity increases with an increase of the coprecipitating pH initially and thereafter decreases. The NPs prepared with a 1.5% NH₄OH solution (LHO-S1.5, pH = 12.1) display a maximum violetblue emission intensity, which is related to its optimum particle size, surface area, and crystallinity. The XRD and surface area measurements confirmed that the particle size increases but the

surface area decreases from LHO-S0.75 to LHO-S7.5. Smaller surface area samples have fewer surface defects, and therefore the probability of nonradiative relaxation decreases, which leads to higher emission intensity. 40,63 As the coprecipitating pH value is further increased, although the surface defects decrease, the effect of the incorporated hydroxyl ions into the NPs predominates that of the decreased surface defects (Table S1). Hydroxyl ions are known to provide additional pathways for nonradiative relaxation, and therefore the emission intensity decreases.⁶⁴ The luminescence lifetime decay profile for the La₂Hf₂O₇ NPs prepared with various pH values is shown in Figure 4c. For samples LHO-S0.75 and LHO-S1.5, the lifetime value does not change much ($\tau \sim 9.6 \ \mu s$), whereas there is a slight enhancement for LHO-S3 and other samples to 10.0 μ s. The CIE color coordinate of a luminescent material is a very important photophysical parameter for qualifying the material used as a phosphor. A CIE chromaticity diagram for the La₂Hf₂O₇ NPs is shown in Figure 4d. The CIE coordinate values obtained for the LHO-S0.75 sample were found to be 0.168 and 0.85, showing a strong violet-blue emitter. The CIE index diagram shown in Figure 4d clearly shows that the color emitted by the NPs changes slightly in the domain of bluishindigo to bluish-violet from LHO-S0.75 to LHO-S7.5. This study projects a probable way to make color tunable nanophosphors simply by changing the coprecipitating pH during the synthesis.

3.3.3. PL Properties of the La₂Hf₂O₇:Eu³⁺ NPs. Figure 5a shows the PL excitation (PLE) spectra of the La₂Hf₂O₇:Eu³⁺ NPs prepared with various coprecipitation pH values. There is a very broad band in the range of 230-330 nm and relatively weaker features in the range from 350 to 550 nm. Chargetransfer bands (CTBs) can arise from three different mechanisms: (i) a host absorption band (HAB) due to O²⁻ → Hf⁴⁺ charge transfer; (ii) intervalence charge transfer due to $Hf^{4+} \rightarrow Eu^{3+}$ charge transfer; (iii) a CTB due to $O^{2-} \rightarrow Eu^{3+}$ charge transfer. Such broadness in the CTB could most likely arise through contributions from all three types of electronic transitions, although the major contribution to the CTB would be from $O^{2-} \rightarrow Eu^{3+}$ electron transfer. The weaker spectral features in the range of 350-550 nm originated from direct excitation of the f-f transitions of Eu³⁺. Among them, the most intense peak at 395 and 464 nm are attributed to ${}^{7}F_{0} \rightarrow {}^{5}L_{6}$ and ${}^{7}F_{0} \rightarrow {}^{5}D_{2}$ transitions, respectively. Figure 5b shows variation in the PLE intensity (the CTB as well as the f-f band as a function of the coprecipitating pH). It can be seen that that the LHO-S1.5 sample has the highest PLE intensity.

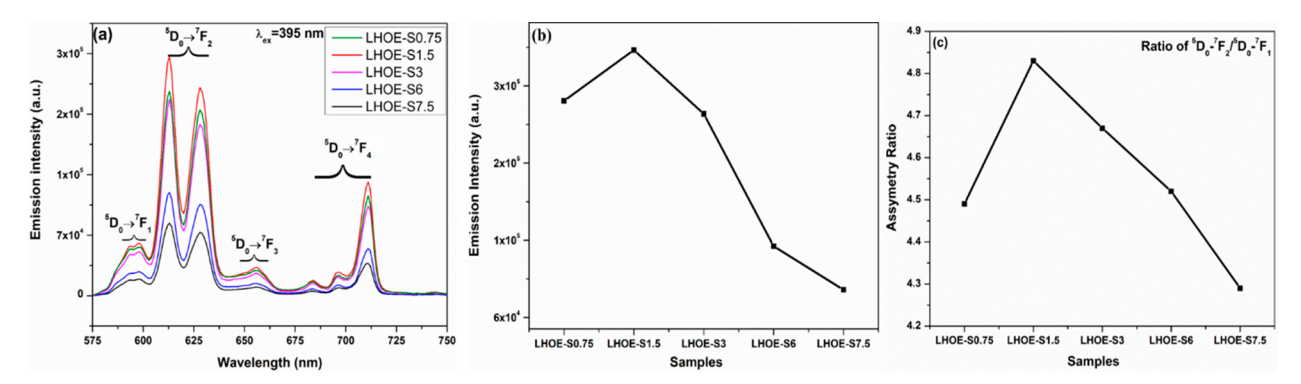


Figure 6. (a) Emission spectra and variations of the (b) emission intensity and (c) asymmetry ratio as a function of the coprecipitating pH of the LHOE NPs.

Interestingly, from Figure 5c, we can see a red shift in the CTB maxima upon going from the LHOE-S0.75 sample to the LHOE-S1.5 sample, but thereafter a blue shift can be seen as the coprecipitating pH increases (LHOE-S1.5 to LHO-S7.5). Such a blue shift in the CTB upon going from low to high pH of the precipitation solution can be attributed to a change in the electronegativity difference between the oxygen and europium ions. This may be due to a change in the electronic environment around the europium ion at higher pH. A similar observation has been seen in other europium-doped phosphors such as YPO₄:Eu and SrMoO₄:Eu. Ningthoujam et al. successfully explained this observation based on the Jorgenson formulation. 65,66 It may happen that the electronegative difference between the europium and oxygen ions decreases and therefore the CTB downsizes to lower wavelength with an increase of the precipitating pH.

On the basis of the expression formulated by Jorgensen,⁶⁷ one can also predict the charge-transfer energy using eq 1:

$$E^{\rm CT} = 3.72(\chi_{\rm X} - \chi_{\rm M}) \text{ eV}$$
 (1)

where χ_X is the optical electronegativity of the anion X from where the electron is transferred and χ_M is the optical electronegativity of the metal M to where the electron is transferred.

Figure 6a shows the emission spectra of the LHOE NPs. In Eu³⁺-doped phosphors, the $^5D_0 \rightarrow {}^7F_1 (\Delta J = \pm 1)$ transition is known as a magnetic-dipole transition (MDT), while the ⁵D₀ \rightarrow ⁷F₂ transition ($\Delta I = \pm 2$) is a forced/hypersensitive electricdipole transition (EDT). The EDT is only allowed when the local symmetry around the Eu3+ ion is very low with no inversion center. Thus, the intensity ratio $I_{D_0 \to {}^7F_2}/I_{D_0 \to {}^7F_1}$ is known as the asymmetry ratio (I_{21}) . It serves as an effective spectroscopic probe of the site symmetry in which the Eu³⁺ ions are situated. That is to say, the higher the ratio, the lower the site symmetry. The excitation intensity of the f-f band is much weaker than that of the CTB, from the commercial viability and the fact that the information deciphered from excitation of an europium ion at 395 nm is more reliable and informative than CTB excitation of the host.⁶⁸ Therefore, we used excitation at 395 nm to obtain emission and lifetime spectroscopy of the LHOE samples.

Upon excitation at 395 nm, there are four prominent peaks seen in the emission spectra of the LHOE samples arising from the ${}^5\mathrm{D}_0 \to {}^7\mathrm{F}_J$ ($J = 0{-}4$) transitions. The peaks at 592 and 612 nm arise from the ${}^5\mathrm{D}_0 \to {}^7\mathrm{F}_1$ ($\Delta J = \pm 1$) and ${}^5\mathrm{D}_0 \to {}^7\mathrm{F}_2$ ($\Delta J = \pm 2$) transitions and are called the MDT and forced/hypersensitive EDT, respectively. The peak around 653 nm

from the ${}^5D_0 \rightarrow {}^7F_3$ transition is not allowed by either MDT or EDT. On the other hand, the peak positioned at around 711 nm is from the ${}^5D_0 \rightarrow {}^7F_4$ transition and is allowed by EDT. Moreover, when rare-earth ions are doped in a coordinating environment, such as a crystal or an inorganic or organic ligand, the individual *I* levels are split up further by the electric field of the host matrix, which is usually referred to as the crystal field. In our case here, as a result of the crystal-field effect induced by the lanthanum hafnate host, these peaks undergo stark splitting, which results in multiple peaks in all of these transitions due to the low actual symmetry around the europium ion. These splittings are usually small ($\sim 100 \text{ cm}^{-1}$) and, depending on the spectral resolution of the fluorimeter used, could appear as fine structures on their individual bands. Often some of these fine structures give information about the symmetry of the coordination environment. For the ${}^5D_0 \rightarrow {}^7F_1$ transition, there are two stark components positioned around 593 and 598 nm. For the $^5D_0 \rightarrow {^7F_2}$ transition, there are two stark components at 612 and 627 nm. For the $^5D_0 \rightarrow {}^7F_4$ transition, there are three stark components at 683, 697, and 711 nm. However, the stark splitting does not have much effect on the $^5D_0 \rightarrow ^7F_3$ transition. The $^5D_0 \rightarrow ^7F_2$ transition with the highest intensity indicates

that Eu3+ is located at a low symmetry without an inversion center. From the results of the XRD/Raman, the LHOE NPs adopt an OP structure with a space group of $Fd\overline{3}m$ and the site symmetry for the La³⁺/Hf⁴⁺ site is D_{3d} . In the OP structure, lanthanum ions exist in 8-fold coordination in a highly distorted scalenohedron, whereas hafnium ions exist in 6-fold coordination in an ideal octahedron. The site symmetry around the Eu³⁺ ion is very low (EDT at 613 nm is very intense compared to MDT at 592 nm). This fact indicates that most of the Eu³⁺ ions are localized at a highly distorted LaO₈ scalenohedron. The substitution of Eu³⁺ for Hf⁴⁺ causes defect formation (oxygen vacancy) in the host lattice because the hafnium site is too small to accommodate a large europium ion. Combined with the distorted symmetry at the LaO₈ scalenohedron, the site symmetry of Eu³⁺ ions deviates from the actual D_{3d} symmetry. So, the red emission of the Eu³⁺ ions from the ${}^5D_0 \rightarrow {}^7F_2$ transition dominates the emission spectra of the LHOE NPs with high asymmetry ratio values in the range of 4.4-4.8. This is further justified using a cohesive energy calculation of Eu³⁺ and LaO₈ and HfO₆ sites using DFT calculations in section 3.3.4.

Under excitation with near-UV light, the equilibrium geometry of ground- and excited-state wave functions of lanthanide ions residing in our $La_2Hf_2O_7$ NPs remains the

same. Therefore, we could not see changes in the peak position from our samples prepared at different pH values, but a change of the relative peak intensity was observed in Figure 6. The emission intensity variation in the LHOE samples (Figure 6b) is consistent with the results observed from the LHO samples (Figure 4b). As the particle size increases from sample LHOE-S0.75 to sample LHOE-S7.5, the surface defect decreases and the emission intensity increases. The LHOE-S1.5 sample presents the most intense red emission at 613 nm due to its high crystallinity and low surface defect density. After sample LHOE-S1.5, there is a progressive decrease in the PL emission intensity, which is attributed to the enhanced role of the hydroxyl ion than surface defect. The pronounced hard acid character of Eu3+ indicates that it will bind strongly to hard bases like water (H₂O) and hydroxyl ions (OH⁻). When solvents containing OH bind to europium ions, 5D0-level decay is emitted nonradiatively through weak vibronic coupling with the vibrational levels of the O-H oscillators. Especially, the bonds with hydrogen have a small reduced mass and therefore exhibit high vibrational energy. These bonds therefore are able to take up a large amount of vibrational energy and effectively quench lanthanide fluorescence from ions with large separation between the emitting energy levels. Eu³⁺ ions have large energy gaps between the emissive ⁵D₀ and ⁵D₄ states of 12000 cm⁻¹, but their luminescence can still be quenched substantially when they are subjected to water (high vibrational energy: $\nu_{\rm max} \sim 3500~{\rm cm}^{-1}$).

Figure 6c shows variation of the asymmetry ratio as a function of the coprecipitating pH value used. It can be seen that I_{21} initially increases to the LHOE-S1.5 sample and thereafter decreases. This indicates that the local environment around Eu3+ ions in the LHOE-S1.5 NPs is the most asymmetric. This may be because the La Porte selection rule for the f-f transition is relaxed to a maximum extend in the LHOE-S1.5 sample, so it exhibits the highest emission intensity. The systematic decrease in I_{21} thereafter because the extent of distortion around Eu³⁺ at 8-coordinated La³⁺ and 6-coordinated Hf⁴⁺ sites decreases in the LHOE NPs. This can also be attributed to the fact that the structures of the LHOE NPs become more and more ordered (ideal pyrochlore) as the coprecipitating pH of the LHOE samples is raised. This phenomenon is well consistent with the results from the Raman spectra (Figure S8), wherein peak narrowing is observed at higher coprecipitating pH. Therefore, the extent of ordering in these LHOE NPs increases as the coprecipitating pH is raised. At low coprecipitating pH, both of the prepared LHO and LHOE NPs have some lattice disordering.

The QY was measured for the LHOE NPs in a Teflon-coated integration sphere to study the effect of the coprecipitating pH controlled by the concentration of the added NH₄OH solution on the light emission efficiency. Table 2 shows the QY value of the as-prepared LHOE NPs under 258 nm excitation. The QY value initially increases and then

Table 2. PL QY for the LHOE NPs at Room Temperature under 258 nm Excitation after Intensity Integration of the PL Emission Ranging from 500 to 750 nm

sample	QY (%)	sample	QY (%)
LHOE-S0.75	16.18	LHOE-S6	15.93
LHOE-S1.5	19.43	LHOE-S7.5	15.15
LHOE-S3	16.81		

decreases, which is in line with the emission intensity trend (Figure 6). The initial increase is attributed to the reduction of surface defects (due to an increase in the particle size), and thereafter QY reduction is due to quenching by the incorporation of more hydroxyl ions at higher coprecipitating pH. When the particle size gets bigger, surface defects reduce, leading to an increase in the QY, as observed from LHOE-S0.75 to LHOE-S1.5. Then the surface defects ultimately act as nonradiative channels to quench luminescence.

3.3.4. Feasibility of Host-to-Dopant Energy Transfer and the Origin of Luminescence in the LHOE NPs: A DFT Study. Figure S10 shows emission spectra of the LHOE NPs in the region of 350–725 nm. From these spectra, we could not find the presence of the host emission in any of these samples, indicating efficient energy transfer from host to dopant. However, in some cases, there is the absence of host-to-dopant energy transfer. ^{12,69,70} To understand the fundamental mechanism that governs the host-to-dopant ETP in the LHOE NPs, we carried out DFT calculations in the doped LHOE samples.

Figure 7a shows our DFT-GGA-calculated total- and angular-momentum-decomposed DOSs of europium doped in an ideal LHO in La site. Eu d states are distributed throughout the VB and contribute majorly at the bottom of the VB. Strong bonding between the O 2p and Eu 5d states can be identified at the bottom of the VB. The antibonding states of Eu 5d are located in the CB region. The 5d states are present in the VB and CB regions in both spin components. The top part of the VB is mainly contributed by the Eu f states in the majority spin component. The CB is dominated by the minority spin component of the Eu f states. Therefore, a close agreement in the distribution of d and f states of Eu³⁺ in the VB/CB energy region of LHO makes it feasible for optical energy transfer between the LHO host and dopant Eu³⁺ ions. In emission spectra of the LHOE NPs (Figure S9), no emission peaks are present in the 350-450 nm region, signifying energy transfer from the LHO host to europium dopant.

Figure 7b shows the DOSs of europium-doped LHO at the lanthanum site and in the presence of an oxygen vacancy in charge state 1+ $({\rm V_O}^{1+})$. In the undoped ${\rm V_O}^{1+}$ case, two impurity states were present in the band gap [Figure 6A(c)], and the occupied (unoccupied) impurity state present below (above) the Fermi energy was contributed by the majority spin component (minority spin component). However, in the europium-doped case, the Eu f states are contributing to the impurity states in both the majority and minority spin components. Moreover, at defect states, the degeneracies of the Eu f states are lifted because the majority and minority spin components are present at different energies for the same defect state.

Figure 7c shows the DOSs of europium-doped LHO at a lanthanum site and in the presence of an oxygen vacancy in charge state 2+ $({\rm V_O}^{2+})$. Because of europium doping, new impurity levels appeared just above the VB maximum in the majority spin component. Most importantly, the degeneracy of the impurity states (located in the band-gap region) was present for the ${\rm V_O}^{2+}$ case, which is lifted because of europium doping in the lanthanum site. As a result, the defect states corresponding to the majority and minority spin components are present at different energies for the defect states present at the center of the band gap. Moreover, the defect states present

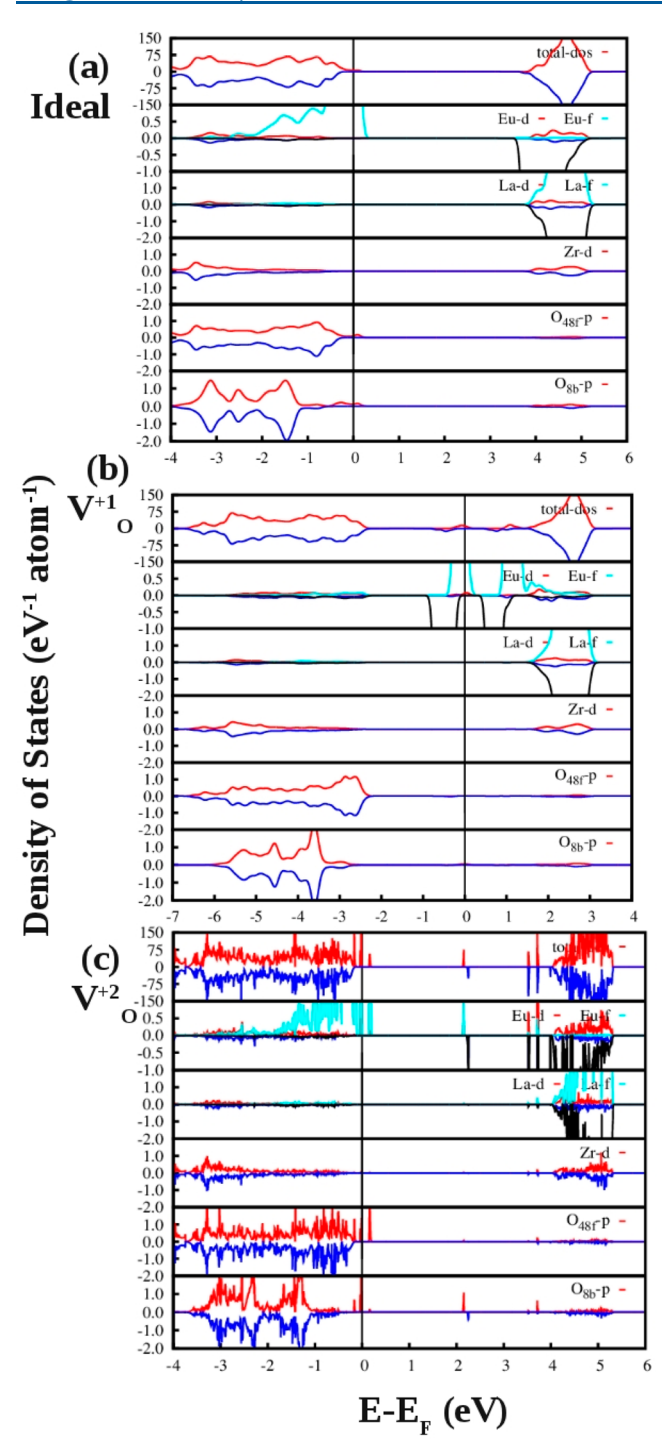


Figure 7. DFT–GGA-calculated total- and angular-momentum-decomposed DOSs of (a) an ideal pyrochlore $\text{La}_2\text{Hf}_2\text{O}_7$ with europium doping, (b) europium-doped LHO with an oxygen vacancy of charge $1+(V_0^{-1+})$, and (c) europium-doped LHO with anoxygen vacancy of charge $2+(V_0^{-2+})$. The vertical lines at 0 eV present the Fermi energy. Europium doping was made in the lanthanum site in all cases.

near the CB minimum are split up into two separate defect states in both the majority and minority spin components.

Figure 6a shows PL emission spectra of the LHOE NPs that have the most intense peaks at 613 and 630 nm due to the 5D_0 \rightarrow 7F_2 EDT. We believe the origin of those peaks is mediated through the V_0^{1+} and V_0^{2+} states. Consistently, Figure 7 shows that Eu³⁺ doping at the lanthanum site lifts the degeneracy

between the majority/minority spin components and Eu f states are present at the defect energy levels in both spin components. The Eu 5d states are distributed throughout the VB. Therefore, transitions between the d states (present in the VB) and f states (present in the defect states) give rise to the intense europium emission.

To understand the structural substitution of Eu³⁺ in the LHO host at LaO₈ or HfO₆ polyhedra following our discussion of Figure 6a, the cohesive energies of europium-doped LHO were calculated for europium doping at the lanthanum and hafnium sites. Our calculations considered a level of europium doping of ¹/₈₈ (1.136%) in LHO, and full structural relaxations were performed as described in the methodology section. Our DFT calculations show that the La³⁺ site is energetically more favorable than the Hf4+ site, implying preferential occupation of europium atoms at the lanthanum sites. The Hf-O and Eu-O bond distances in HfO₆ and EuO₆ are 2.10 and 2.26 Å, respectively. Europium doping in HfO₆ polyhedra increases the bond distances by 7.6%. The La-O bond distances in LaO₈ polyhedra are 2.34 Å (two bonds) and 2.65 Å (six bonds). Europium doping in LaO₈ polyhedra changes the bond distances to 2.26 Å (two bonds) and 2.63 Å (six bonds). Therefore, energetically europium will not go to the hafnium site because the energy difference between europium doping in the lanthanum and hafnium sites is 6.2 eV.

3.3.5. Excited-State Lifetime of the LHOE NPs. The room temperature decay curves of PL emission of the LHOE NPs showed a nonexponential shape, as shown in Figure S11. Therefore, we applied a double-exponential fitting equation that takes into account both the fast and slow components of the decay:

$$I(t) = A_0 + A_1 \exp\left(\frac{-t}{\tau_1}\right) + A_2 \exp\left(\frac{-t}{\tau_2}\right)$$
(2)

where A_0 , A_1 , and A_2 are scalar quantities obtained from the biexponential fitting, t is the time, and τ_1 and τ_2 are the fast and slow decay time values, respectively. It is worth mentioning that this provides a mathematical strategy useful for the calculation of a representative effective lifetime $\tau_{\rm av}$ for each system according to the following equation:

$$\tau_{\rm av} = \frac{A_1 \tau_{\rm f}^2 + A_1 \tau_{\rm s}^2}{A_1 \tau_{\rm f} + A_1 \tau_{\rm s}} \tag{3}$$

As seen from Figure S11 and Table 3, decay curves of the LHOE NPs display two lifetimes, indicating the presence of Eu³⁺ ions in two different environments. The long-lived component with $\tau_2=2.14-2.67$ ms is attributed to the Eu³⁺ ion occupying the La³⁺ site, which are far away from structural defects, whereas the short-lived component with $\tau_1=0.723-1.24$ ms is attributed to the Eu³⁺ ion in the same site but in

Table 3. Luminescence Lifetime Values for the LHOE NPs $(\lambda_{ex} = 395 \text{ nm and } \lambda_{em} = 613 \text{ nm})$

			popu	lation	
sample	$ au_1 \; (ms)$	$\tau_2 \; (ms)$	% τ ₁	% τ ₂	$ au_{\mathrm{avg}}\ (\mathrm{ms})$
LHOE-S0.75	0.723	2.46	22	78	2.14
LHOE-S1.5	0.856	2.48	23	77	2.23
LHOE-S3	1.02	2.58	21	79	2.34
LHOE-S6	1.19	2.71	22	78	2.51
LHOE-S7.5	1.24	2.92	19	81	2.67

closer proximity to structural defects. In addition, it is seen that the average lifetime and long-lived component monotonically increase as the coprecipitating pH raises, unlike the emission intensity and quantum efficiency. As the size of the LHOE NPs increases from LHOE-S0.75 to LHOE-S7.5, the surface area and defects decrease, so the same trend is seen in terms of the lifetime. The lifetime values suggested that the decay time is fastest for the LHOE-S0.75 sample and slowest for the LHOE-S7.5 sample.

3.3.6. RL Properties of the LHOE NPs. To investigate the photophysical properties of the LHOE NPs, their emission spectra were collected with a photomultiplier-tube-coupled spectrograph, wherein the powder samples were irradiated with X-rays coming from a silver source (12 W; Figure 8). Here the

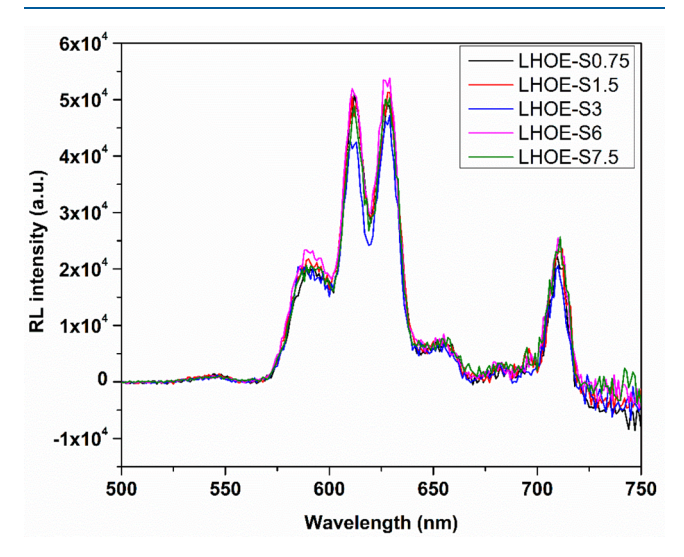


Figure 8. RL spectra of the LHOE NPs.

LHOE NPs act as efficient X-ray absorbers with a K-edge at 22.1 keV, which falls in the range of diagnostic X-ray, because of the high atomic number of hafnium ($Z_{Hf} = 72$) and the high density of LHO (7.9 g cm⁻³). No violet-blue emission of the LHO host could be seen upon X-ray irradiation, indicating efficient host-to-dopant energy transfer. Rather, a small identifiable broad peak could be seen around 550 nm, which could be attributed to X-ray-induced conversion of some of the Eu3+ ions to the divalent ion. Such a phenomenon is also observed in other hosts such as CaAl₂O₄ and Sr₂SiO₄. 71,72 The RL spectral features of these NPs are similar to the PL ones (Figure 6a), consisting of the typical europium ion transition in the range of 580-740 nm with an intense red emission at 612 nm due to the $^5D_0 \rightarrow ^7F_2$ EDT and a MDT band at 592 nm due to the $^5D_0 \rightarrow ^7F_1$ transition. In addition to these, a very intense emission peak at 710 nm due to ${}^5D_0 \rightarrow {}^7F_4$ transitions within the so-called "biological window" could be also

detected. In this near-infrared spectral region, hemoglobin in blood and water/lipids molecules has a minimal absorption coefficient, allowing deeper tissue imaging.⁷³ All of these emission peaks in the LHOE NPs arise from Eu³⁺, which acts as a trap level within the band gap of lanthanum hafnate.⁷⁴ In lanthanide-doped nanophosphors, both ground- and excited-state wave functions governing the f–f transition and also their equilibrium geometries are the same. This is mainly because the f–f transitions are strongly shielded from the outlying 6s² and 5p⁶ shells, which are lower in energy but spatially located outside of the 4f orbital. This unique optical property enables the tunability of the LHOE NPs and allows multiplex imaging by changing the dopant in these nanophosphors.

In addition, there is not much difference in the RL spectra among the different samples, unlike the PL spectra, wherein the LHOE-S1.5 sample displays the maximum quantum efficiency. Also, irradiated by X-ray, the symmetry around the Eu³⁺ ion improves and the asymmetry ratio reduces to 2.5.

3.4. Judd–Ofelt Analysis of the LHOE NPs. All photophysical parameters, such as $A_{\rm R}$, $A_{\rm NR}$, IQE, and JO, and branching ratios of the LHOE NPs are calculated based on the above-mentioned equations and listed in Table 4.

It is well-known that the parameter Ω_2 is an indication of the dominant covalent nature and/or structural changes in the proximity of the Eu³⁺ ion (short-range effects), while Ω_4 intensity parameters are long-range parameters that can be related to the bulk properties such as the viscosity and rigidity of the inorganic matrixes. The Ω_2 parameter is related to the degree of covalence and polarizability of the chemical environment experienced by the Eu³⁺ ion. Higher Ω_2 values point to more covalent and polarizable environments around Eu^{3+} ions in hosts. High values of the Ω_2 parameters can also be related to the high asymmetry of the Eu³⁺ surrounding environment. This is well in agreement with the high asymmetry ratio values of Eu³⁺ in the LHOE NPs. The calculated τ_R (1/ A_R) for the excited-state 5D_0 level of the Eu³⁺ ion is found to be larger than the experimental τ_{av} (Table 4). This difference in au_{exp} and au_{cal} can be attributed to nonradiative decays. The trend in the branching ratio suggests that most of the radiative energy goes into the $^5D_0 \rightarrow {}^7F_2$ transition. The IQE value was also found to be a maximum for the LHOE-S1.5 sample, which further supports our observed luminescence results and QY values (Figure 6a and Table 2). This is attributed to the lowest nonradiative transition rate in the LHOE-S1.5 sample owing to its optimum crystallinity, defect, and hydroxyl ion concentration.

3.5. Thermal Stability of the LHOE NPs. For application in high-power LEDs, the thermal stability of phosphors is one of the important issues to be considered. Therefore, we have explored the thermal stability of the LHOE-S1.5 sample using in situ PL measurements. At room temperature, the material experienced intense red luminescence. However, as the

Table 4. Calculated Judd-Ofelt and Photophysical Parameters of the LHOE NPs (A_R = Radiative Rate, A_{NR} = Nonradiative Rate, Ω = Judd-Ofelt Parameter, and β = Branching Ratio)

sample	$A_{\rm R} \ ({\rm s}^{-1})$	$A_{\rm NR}~(\rm s^{-1})$	IQE (%)	$\Omega_2~(\times 10^{-20})$	$\Omega_4~(imes 10^{-20})$	β_1 (%)	β_2 (%)	β_4 (%)
LHOE-S0.75	292	196.9	59.7	2.30	1.33	17.1	62.7	18.0
LHOE-S1.5	287	96.2	74.9	2.24	1.32	17.4	62.1	18.2
LHOE-S3	286	130.7	68.6	2.23	1.31	17.5	62.1	18.1
LHOE-S6	262	157.7	62.4	2.10	0.98	19.1	63.8	14.8
LHOE-S7.5	285	189.8	60.0	2.23	1.29	17.6	62.2	17.9

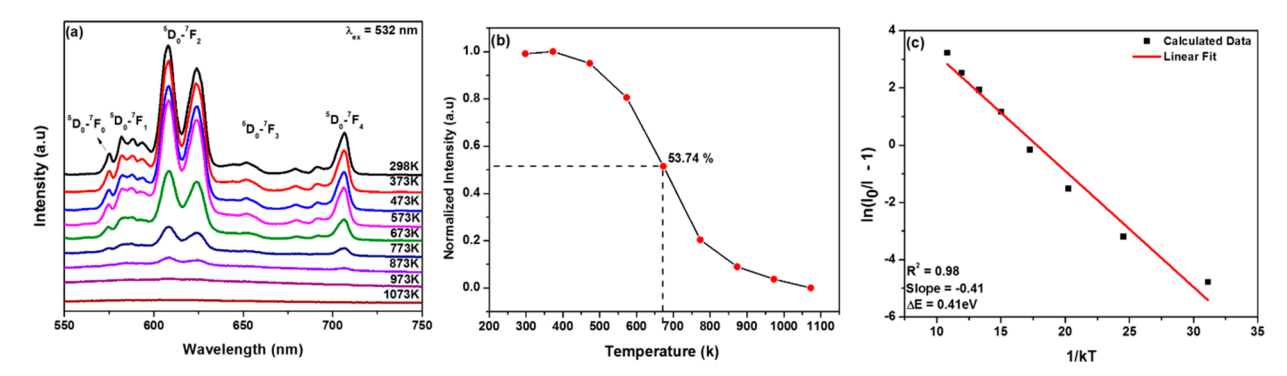


Figure 9. (a) PL emission spectra at temperatures ranging from 298 to 1072 K. (b) Corresponding temperature dependence of the PL emission intensity of the ${}^5D_0 \rightarrow {}^7F_2$ transition. (c) Plot of $\ln(I_0/I - 1)$ versus 1/kT of the LHOE-S1.5 NPs.

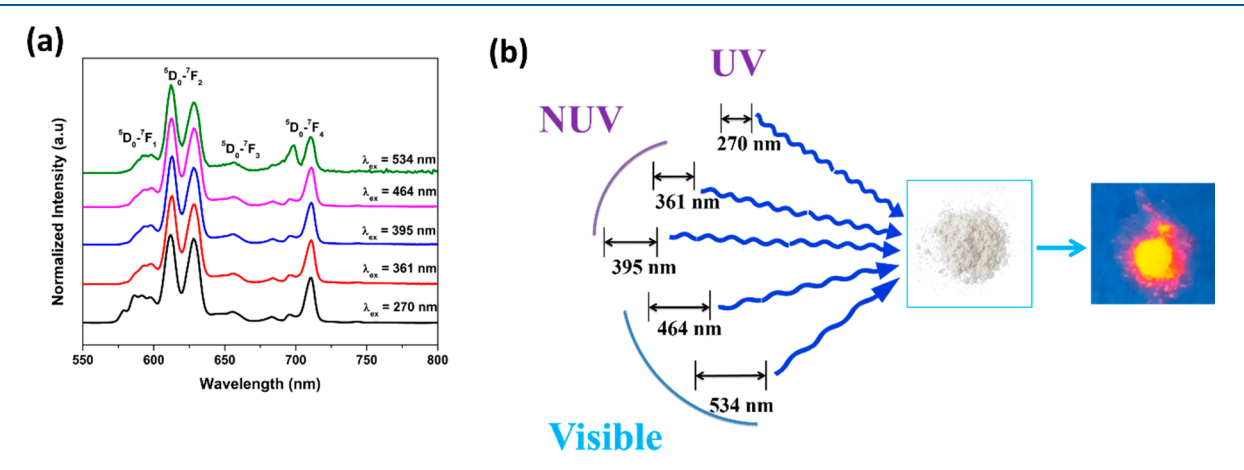


Figure 10. (a) Emission spectra and (b) digital images showing red color emissions of the $La_2Hf_2O_7$: Eu^{3+} (LHOE-S1.5) under UV, near-UV, and visible-light excitation.

temperature increases systematically, the PL intensity output decreases continuously (Figure 9a). Such PL reduction is due to thermal quenching wherein emissive centers are thermally activated through the crossing point between the ground- and excited-state levels. At 673 K, the red emission output of our NPs decreases to 53.74% to the original emission, and at 973 K, it is fully suppressed (Figure 9b). This behavior indicates that the LHOE NPs possess extraordinary thermal stability, and it is suitable for usage as a phosphor in LEDs. In addition, the activation energy of the NPs was extrapolated from the slope of Figure 9c denoted from the following Arrhenius equation:

$$\ln\left(\frac{I_0}{I} - 1\right) = \ln A - \frac{\Delta E}{kT} + C \tag{4}$$

where I_0 expresses the initial PL intensity, I is the PL emission intensity at a given temperature T and a given constant A, ΔE denotes the activation energy involved, and k is the Boltzmann constant. The relationship of $\ln\left(\frac{I_0}{I}-1\right)$ and $\frac{1}{kT}$ holds a linear fit. The slope was computed through linear regression to be -0.41, which is proportional to the involved activation energy of the LHOE-S1.5 NPs. Therefore, the activation energy is equal to 0.41 eV for thermal quenching. In this unique case, the activation energy is superior to the usual value for europium-doped silicate-based red phosphors with $\Delta E \sim 0.23$ eV. The reported activation energies of $La_2Zr_2O_7$:Eu³⁺ and Sr_2MgTeO_6 :Eu³⁺ phosphors for thermal quenching are 0.16 and 0.27 eV, respectively. 45,76 A very high activation energy

value of 0.41 eV supports the fact that other than high QY, good emission and radioluminescent properties, and high lifetime, our LHOE NPs indeed also have excellent thermal stability.

3.6. Exploration of the Lanthanum Hafnate Host for Red-Green-Blue (RGB)-Based White LEDs. From the application perspective, the La₂Hf₂O₇:Eu³⁺ NPs have high potential as red-emitting phosphors in RGB-based white LEDs with a quantum efficiency close to 20%. In addition, these phosphors give intense red emission under near-UV excitation (393 and 465 nm), which is the prerequisite for RGB-based white LEDs (Figure 10).

Our size-tunable $La_2Hf_2O_7$: Eu^{3+} NPs have the ability to be excited by multiple wavelengths, including near-UV (270 nm), violet (361 nm), indigo (395 nm), blue (464 nm), and green (534 nm) light. In all cases, the NPs display emission in the red region, with peaks pertaining to our europium activator. This multiwavelength property is vital for future applications in the white-LED design. White-light engineering today suffers from low color rendering because of the absence of a good, thermally stable red phosphor. In this respect, our material is suitable for white-light engineering.

Moreover, these La₂Hf₂O₇:Eu³⁺ NPs have a high thermal quenching temperature of 673 K and a high activation energy of 0.41 eV, which are high compared to those of other red phosphors. Along with all of these PL properties, they possess the unique ability to give red emission under X-ray excitation, highlighting their potential as X-ray scintillators. Overall, the high QY, high excited-state lifetime, intense RL, and high

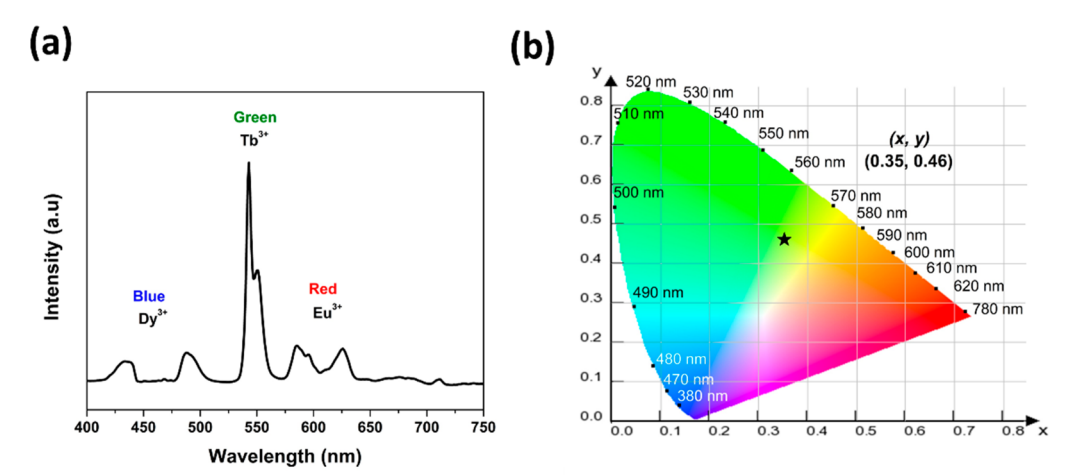


Figure 11. (a) Emission spectrum of the tridoped $La_2Hf_2O_7$: Eu, Tb, Dy NPs under 254 nm excitation. (b) Color coordinate diagram of the tricodoped phosphor.

thermal stability highlight their potential for advanced optoelectronic, radiation detection, and bioimaging applications.

Pertaining to white-light emission, we codoped Tb^{3+} and Dy^{3+} in the $La_2Hf_2O_7$: Eu^{3+} NPs. Stabilization of Dy^{3+} (for blue), Tb^{3+} (for green), and Eu^{3+} (for red) in the $La_2Hf_2O_7$ host can be seen in Figure 11a, where all peaks corresponding to Dy^{3+} , Tb^{3+} , and Eu^{3+} are present. In Figure 11b, the color coordinates from this tridoped system had a value of (0.35, 0.46), which is in the domain of near white light. In future studies, we will focus on optimization of the concentration of all activators to obtain an optimum combination that generates pure white light (CIE = 0.33, 0.33) with high quantum efficiency.

4. CONCLUSION

In this work, we correlated the structure and luminescence of undoped and Eu3+-doped La2Hf2O7 NPs. The extent of ordering in the pyrochlore host increases as the pH of the coprecipitation solution is raised, but structure remained an ideal pyrochlore. DFT calculations showed defect electronic states generated due to charged oxygen defects in the band gap responsible for PL in undoped NPs. The emitted color changes slightly from bluish-indigo to bluish-violet as the pH of the coprecipitation solution goes up. The optimum luminescence efficiency for both undoped and doped samples was found for the sample coprecipitated with 1.5% NH₄OH(aq) owing to its optimum crystallinity, low agglomeration, low hydroxyl ion concentration, and low surface defects. Efficient host-to-dopant energy transfer in the LHOE samples is explained using DOS calculations. The origin of the most intense red emission in the LHOE samples is mediated through Eu f states presented at charged oxygen defect states in the electronic band gap and Eu d states presented at the VB. On the basis of cohesive energy calculations, it is also proposed that europium is energetically more stable at the LaO₈ site. The high QY, high excited-state lifetime, intense RL, and high thermal stability highlight the potential of the synthesized NPs for advanced optoelectronic, radiation detection, and bioimaging applications.

ASSOCIATED CONTENT

S Supporting Information

The Supporting Information is available free of charge on the ACS Publications website at DOI: 10.1021/acs.inorg-chem.8b01983.

Experimental and theoretical sections, XRD patterns, lattice parameters and crystallite sizes, Rietveld refined and relevant structural parameters, scanning and transmission electron microscopy images, elemental mapping and energy-dispersive spectroscopy images, FTIR, Raman, and emission spectra, luminescence decay profiles of the La₂Hf₂O₇NPs, and Judd–Ofelt analysis (PDF)

AUTHOR INFORMATION

Corresponding Author

*E-mail: yuanbing.mao@utrgv.edu. Tel.: +1-956-665-2986.

ORCID 6

Santosh K. Gupta: 0000-0002-1178-0159 Yuanbing Mao: 0000-0003-2665-6676

Notes

The authors declare no competing financial interest.

ACKNOWLEDGMENTS

The authors are thankful for financial support from the National Science Foundation under Award CHE-1710160 and Grant DMR-1523577 and the USDA National Institute of Food and Agriculture (Award 2015-38422-24059, for the Integrating Food Science/Engineering and Education Network program). The Department of Chemistry at the University of Texas Rio Grande Valley is grateful for generous support provided by a Departmental Grant from the Robert A. Welch Foundation (Grant BX-0048). S.K.G. thanks the United States-India Education Foundation and Institute of International Education for his Fulbright Nehru Postdoctoral Fellowship (Award 2268/FNPDR/2017). The in situ PL measurements were conducted at the Center for Nanophase Materials Science, which is a U.S. Department of Energy, Office of Science User Facility, and the authors thank Dr. A. Puretzky for technical assistance. The authors also thank Melonie Thomas for high-resolution transmission electron

microscopy and Enrique Molina for BET surface area measurements.

REFERENCES

- (1) Sibille, R.; Gauthier, N.; Yan, H.; Ciomaga Hatnean, M.; Ollivier, J.; Winn, B.; Filges, U.; Balakrishnan, G.; Kenzelmann, M.; Shannon, N.; Fennell, T. Experimental signatures of emergent quantum electrodynamics in $Pr_2Hf_2O_7$. *Nat. Phys.* **2018**, *14*, 711–715.
- (2) Kim, J.; Shih, P.-C.; Tsao, K.-C.; Pan, Y.-T.; Yin, X.; Sun, C.-J.; Yang, H. High-performance pyrochlore-type yttrium ruthenate electrocatalyst for oxygen evolution reaction in acidic media. *J. Am. Chem. Soc.* **2017**, *139*, 12076–12083.
- (3) Gupta, A.; Kumar, A.; Waghmare, U.; Hegde, M. Activation of oxygen in Ce₂Zr₂O_{7+x} across pyrochlore to fluorite structural transformation: First-principles analysis. *J. Phys. Chem. C* **2017**, *121*, 1803–1808
- (4) Perriot, R.; Uberuaga, B. P.; Zamora, R. J.; Perez, D.; Voter, A. F. Evidence for percolation diffusion of cations and reordering in disordered pyrochlore from accelerated molecular dynamics. *Nat. Commun.* **2017**, *8*, 618.
- (5) Pokhrel, M.; Wahid, K.; Mao, Y. Systematic studies on $RE_2Hf_2O_7$:5% $Eu^{3+}(RE=\ Y,\ La,\ Pr,\ Gd,\ Er,\ and\ Lu)$ nanoparticles: effects of the A-site RE^{3+} cation and calcination on structure and photoluminescence. *J. Phys. Chem. C* **2016**, *120*, 14828–14839.
- (6) Zhao, Y.; Yang, W.; Li, N.; Li, Y.; Tang, R.; Li, H.; Zhu, H.; Zhu, P.; Wang, X. Pressure-enhanced insulating state and trigonal distortion relaxation in geometrically frustrated pyrochlore Eu₂Sn₂O₇. *J. Phys. Chem. C* **2016**, *120*, 9436–9442.
- (7) Zuniga, J. P.; Gupta, S. K.; Pokhrel, M.; Mao, Y. Exploring the optical properties ofLa₂Hf₂O₇:Pr³⁺ nanoparticles under UV and X-ray excitation for potential lighting and scintillating applications. *New J. Chem.* **2018**, *42*, 9381–9392.
- (8) Sachan, R.; Cooper, V. R.; Liu, B.; Aidhy, D. S.; Voas, B. K.; Lang, M.; Ou, X.; Trautmann, C.; Zhang, Y.; Chisholm, M. F.; Weber, W. J. Forging fast ion conducting nanochannels with swift heavy ions: the correlated role of local electronic and atomic structure. *J. Phys. Chem. C* 2017, 121, 975–981.
- (9) Pokhrel, M.; Burger, A.; Groza, M.; Mao, Y. Enhance the photoluminescence and radioluminescence of $La_2Zr_2O_7$: Eu^{3+} core nanoparticles by coating with a thin Y_2O_3 shell. *Opt. Mater.* **2017**, *68*, 35–41.
- (10) Tang, Z.; Huang, Z.; Qi, J.; Guo, X.; Han, W.; Zhou, M.; Peng, S.; Lu, T. Synthesis and characterization of $Gd_2Zr_2O_7$ defect-fluorite oxide nanoparticles via a homogeneous precipitation-solvothermal method. *RSC Adv.* **2017**, *7*, 54980–54985.
- (11) Zhang, Y.-W.; Si, R.; Liao, C.-S.; Yan, C.-H.; Xiao, C.-X.; Kou, Y. Facile alcohothermal synthesis, size-dependent ultraviolet absorption, and enhanced CO conversion activity of ceria nanocrystals. *J. Phys. Chem. B* **2003**, *107*, 10159–10167.
- (12) Gupta, S. K.; Ghosh, P. S.; Yadav, A. K.; Jha, S. N.; Bhattacharyya, D.; Kadam, R. M. Origin of blue-green emission in α - $Zn_2P_2O_7$ and local structure of Ln^{3+} Ion in α - $Zn_2P_2O_7$: Ln^{3+} (Ln= Sm, Eu): Time-resolved photoluminescence, EXAFS, and DFT measurements. *Inorg. Chem.* **2017**, *56*, 167–178.
- (13) Gupta, S. K.; Sudarshan, K.; Ghosh, P. S.; Mukherjee, S.; Kadam, R. M. Doping-induced room temperature stabilization of metastable β -Ag₂WO₄ and origin of visible emission in α -and β -Ag₂WO₄: low temperature photoluminescence studies. *J. Phys. Chem.* C **2016**, 120, 7265–7276.
- (14) Pathak, N.; Gupta, S. K.; Prajapat, C.; Sharma, S.; Ghosh, P.; Kanrar, B.; Pujari, P.; Kadam, R. Defect induced ferromagnetism in MgO and its exceptional enhancement upon thermal annealing: a case of transformation of various defect states. *Phys. Chem. Chem. Phys.* **2017**, *19*, 11975–11989.
- (15) Gupta, S. K.; Ghosh, P.; Sudarshan, K.; Gupta, R.; Pujari, P.; Kadam, R. Multifunctional pure and Eu^{3+} doped β -Ag₂MoO₄: photoluminescence, energy transfer dynamics and defect induced properties. *Dalton Trans* **2015**, *44*, 19097–19110.

- (16) Zhang, F.; Wang, J.; Lian, J.; Lang, M.; Becker, U.; Ewing, R. Phase stability and pressure dependence of defect formation in $Gd_2Ti_2O_7$ and $Gd_2Zr_2O_7$ pyrochlores. *Phys. Rev. Lett.* **2008**, *100*, 045503
- (17) Gupta, S. K.; Sudarshan, K.; Ghosh, P.; Srivastava, A.; Bevara, S.; Pujari, P.; Kadam, R. Role of various defects in the photoluminescence characteristics of nanocrystalline Nd₂Zr₂O₇. an investigation through spectroscopic and DFT calculations. *J. Mater. Chem. C* **2016**, *4*, 4988–5000.
- (18) Lian, J.; Wang, L.; Wang, S.; Chen, J.; Boatner, L.; Ewing, R. Nanoscale manipulation of pyrochlore: new nanocomposite ionic conductors. *Phys. Rev. Lett.* **2001**, *87*, 145901.
- (19) Sala, G.; Gutmann, M.; Prabhakaran, D.; Pomaranski, D.; Mitchelitis, C.; Kycia, J.; Porter, D.; Castelnovo, C.; Goff, J. Vacancy defects and monopole dynamics in oxygen-deficient pyrochlores. *Nat. Mater.* **2014**, *13*, 488.
- (20) Carbonio, R. E.; Alonso, J. A.; Martinez, J. Oxygen vacancy control in the defect pyrochlore: a way to tune the electronic bandwidth. *J. Phys.: Condens. Matter* **1999**, *11*, 361.
- (21) Brixner, L. Structural and luminescent properties of the Ln₂Hf₂O₇-type rare earth hafnates. *Mater. Res. Bull.* **1984**, *19*, 143–149.
- (22) Wahid, K.; Pokhrel, M.; Mao, Y. Structural, photoluminescence and radioluminescence properties of Eu³⁺ doped La₂Hf₂O₇ nanoparticles. *J. Solid State Chem.* **2017**, 245, 89–97.
- (23) Hansel, R. A.; Desai, S.; Allison, S. W.; Heyes, A.; Walker, D. G. Emission lifetimes of europium-doped pyrochlores for phosphor thermometry. *J. Appl. Phys.* **2010**, *107*, 016101.
- (24) Sun, M.; Huang, B. Comparison and correlation of structural disorder caused by anion Frenkel in affecting ion conduction of La₂Hf₂O₇ and La₂Mo₂O₉ as high performance electrolytes in SOFCs. *MRS Adv.* **2017**, *2*, 3317–3322.
- (25) Eagleman, Y.; Weber, M.; Chaudhry, A.; Derenzo, S. Luminescence study of cerium-doped $\text{La}_2\text{Hf}_2\text{O}_7$: Effects due to trivalent and tetravalent cerium and oxygen vacancies. *J. Lumin.* **2012**, 132, 2889–2896.
- (26) Eagleman, Y.; Weber, M.; Derenzo, S. Luminescence study of oxygen vacancies in lanthanum hafnium oxide, La₂Hf₂O₇. *J. Lumin.* **2013**, 137, 93–97.
- (27) Gu, S.; Zhang, S.; Xu, D.; Li, W.; Yan, J. Evolution of microstructure and hot corrosion performance of $La_2Hf_2O_7$ ceramic in contact with molten sulfate-vanadate salt. *Ceram. Int.* **2018**, *44*, 2048–2057.
- (28) Gu, S.; Zhang, S.; Xue, B.; Yan, J.; Li, W.; Zhang, L. Phase variation and thermophysical properties of $La_2Hf_2O_7$ with alumina addition. *J. Eur. Ceram. Soc.* **2018**, 38, 1938–1945.
- (29) Sevast'yanov, V. G.; Simonenko, E. P.; Simonenko, N. P.; Sakharov, K. A.; Kuznetsov, N. T. Synthesis of finely dispersed La₂Zr₂O₇, La₂Hf₂O₇, Gd₂Zr₂O₇ and Gd₂Hf₂O₇ oxides. *Mendeleev Commun.* **2013**, 23, 17–18.
- (30) Vecht, A.; Gibbons, C.; Davies, D.; Jing, X.; Marsh, P.; Ireland, T.; Silver, J.; Newport, A.; Barber, D. Engineering phosphors for field emission displays. *J. Vac. Sci. Technol., B: Microelectron. Process. Phenom.* 1999, 17, 750–757.
- (31) Gupta, S. K.; Sudarshan, K.; Ghosh, P.; Sanyal, K.; Srivastava, A.; Arya, A.; Pujari, P.; Kadam, R. Luminescence of undoped and Eu³⁺ doped nanocrystalline SrWO₄ scheelite: time resolved fluorescence complimented by DFT and positron annihilation spectroscopic studies. *RSC Adv.* **2016**, *6*, 3792–3805.
- (32) Wang, W.-N.; Widiyastuti, W.; Wuled Lenggoro, I.; Oh Kim, T.; Okuyama, K. Photoluminescence optimization of luminescent nanocomposites fabricated by spray pyrolysis of a colloid-solution precursor. *J. Electrochem. Soc.* **2007**, *154*, J121–J128.
- (33) Jung, K. Y.; Lee, C. H.; Kang, Y. C. Effect of surface area and crystallite size on luminescent intensity of Y₂O₃:Eu phosphor prepared by spray pyrolysis. *Mater. Lett.* **2005**, *59*, 2451–2456.
- (34) Shea, L.; McKittrick, J.; Phillips, M. Predicting and modeling the low-voltage cathodoluminescent efficiency of oxide phosphors. *J. Electrochem. Soc.* **1998**, *145* (9), 3165–3170.

(35) Shea, L. E.; McKittrick, J.; Lopez, O. A.; Sluzky, E. Synthesis of red-emitting, small particle size luminescent oxides using an optimized combustion process. *J. Am. Ceram. Soc.* **1996**, *79*, 3257–3265.

- (36) Wang, W.-N.; Widiyastuti, W.; Ogi, T.; Lenggoro, I. W.; Okuyama, K. Correlations between crystallite/particle size and photoluminescence properties of submicrometer phosphors. *Chem. Mater.* **2007**, *19*, 1723–1730.
- (37) Gipson, K.; Kucera, C.; Stadther, D.; Stevens, K.; Ballato, J.; Brown, P. The influence of synthesis parameters on particle size and photoluminescence characteristics of ligand capped Tb³⁺:LaF₃. *Polymers* **2011**, *3*, 2039–2052.
- (38) Kahouadji, B.; Guerbous, L.; Boukerika, A.; Dolić, S. D.; Jovanović, D. J.; Dramićanin, M. D. Sol gel synthesis and pH effect on the luminescent and structural properties of YPO₄:Pr³⁺ nanophosphors. *Opt. Mater.* **2017**, *70*, 138–143.
- (39) Ningombam, G. S.; Nongmaithem, R. S. Morphology and photoluminescence of self-assembled CaWO₄:Sm³⁺ microspheres: effect of pH and surfactant concentration. *Int. Nano Lett.* **2017**, *7*, 133–140.
- (40) Tong, S.; Zhao, J.; Wen, X. Preparation and properties of Pr³⁺/Ce³⁺:YAG phosphors using triethanolamine as dispersant and pH regulator. *Bull. Mater. Sci.* **2016**, *39*, 1515–1519.
- (41) Mao, Y.; Guo, X.; Huang, J. Y.; Wang, K. L.; Chang, J. P. Luminescent nanocrystals with $A_2B_2O_7$ composition synthesized by a kinetically modified molten salt method. *J. Phys. Chem. C* **2009**, *113*, 1204–1208.
- (42) Mao, Y.; Park, T. J.; Zhang, F.; Zhou, H.; Wong, S. S. Environmentally friendly methodologies of nanostructure synthesis. *Small* **2007**, *3*, 1122–1139.
- (43) He, C.; Ji, H.; Huang, Z.; Zhang, X.; Liu, H.; Liu, S.; Liu, Y.; Fang, M.; Wu, X.; Min, X. Preparation and photoluminescence properties of red-emitting phosphor ZnAl₂O₄: Eu³⁺ with an intense $^5D_0 \rightarrow ^7F_2$ transition. *Mater. Res. Express* **2018**, *5*, 025501.
- (44) Li, H.; Fang, M.; Huang, Z.; Liu, Y.; Zhu, H.; Min, X.; Zhang, L. Energy transfer mechanism and color-tunable luminescence properties of Eu³⁺-doped BaMg₂V₂O₈ vanadate phosphors. *Chem. Phys. Lett.* **2016**, *662*, 86–90.
- (45) Min, X.; Sun, Y.; Kong, L.; Guan, M.; Fang, M.; Liu, Y. g.; Wu, X.; Huang, Z. Novel pyrochlore-type La₂Zr₂O₇:Eu³⁺ red phosphors: Synthesis, structural, luminescence properties and theoretical calculation. *Dyes Pigm.* **2018**, *157*, 47–54.
- (46) Zhu, H.; Fang, M.; Huang, Z.; Liu, Y.; Chen, K.; Min, X.; Mao, Y.; Wang, M. Photoluminescence properties of Li₂Mg₂(WO₄)₃:Eu³⁺ red phosphor with high color purity for white LEDs applications. *J. Lumin.* **2016**, *172*, 180–184.
- (47) Wang, H.; Gao, L.; Niihara, K. Synthesis of nanoscaled yttrium aluminum garnet powder by the co-precipitation method. *Mater. Sci. Eng., A* **2000**, 288, 1–4.
- (48) McCauley, R. A. Infrared-absorption characteristics of the pyrochlore structure. *J. Opt. Soc. Am.* **1973**, *63*, 721–725.
- (49) Subramanian, M.; Aravamudan, G.; Subba Rao, G. Oxide pyrochlores—a review. *Prog. Solid State Chem.* **1983**, *15*, 55–143.
- (50) Wang, Z.; Zhu, H.; Ai, L.; Liu, X.; Lv, M.; Wang, L.; Ma, Z.; Zhang, Z. Catalytic combustion of soot particulates over rare-earth substituted $\rm Ln_2Sn_2O_7$ pyrochlores (Ln= La, Nd and Sm). *J. Colloid Interface Sci.* **2016**, 478, 209–216.
- (51) Turner, K. M.; Rittman, D. R.; Heymach, R. A.; Tracy, C. L.; Turner, M. L.; Fuentes, A. F.; Mao, W. L.; Ewing, R. C. Pressure-induced structural modifications of rare-earth hafnate pyrochlore. *J. Phys.: Condens. Matter* **2017**, *29*, 255401.
- (52) Garg, N.; Pandey, K.; Murli, C.; Shanavas, K.; Mandal, B. P.; Tyagi, A.; Sharma, S. M. Decomposition of lanthanum hafnate at high pressures. *Phys. Rev. B: Condens. Matter Mater. Phys.* **2008**, *77*, 214105.
- (53) Blanchard, P. E.; Liu, S.; Kennedy, B. J.; Ling, C. D.; Avdeev, M.; Aitken, J. B.; Cowie, B. C.; Tadich, A. Investigating the local structure of lanthanoid hafnates Ln₂Hf₂O₇ via diffraction and spectroscopy. *J. Phys. Chem. C* **2013**, *117*, 2266–2273.

- (54) Gupta, S. K.; Ghosh, P.; Reghukumar, C.; Pathak, N.; Kadam, R. Experimental and theoretical approach to account for green luminescence from $Gd_2Zr_2O_7$ pyrochlore: exploring the site occupancy and origin of host-dopant energy transfer in $Gd_2Zr_2O_7$: Eu³⁺. RSC Adv. **2016**, 6, 44908–44920.
- (55) Zhang, A.; Lü, M.; Yang, Z.; Zhou, G.; Zhou, Y. Systematic research on RE₂Zr₂O₇ (RE= La, Nd, Eu and Y) nanocrystals: Preparation, structure and photoluminescence characterization. *Solid State Sci.* **2008**, *10*, 74–81.
- (56) Slifka, A.; Filla, B.; Phelps, J.; Bancke, G.; Berndt, C. Thermal conductivity of a zirconia thermal barrier coating. *J. Therm. Spray Technol.* **1998**, *7*, 43–46.
- (57) Anderson, M. D.; Stevenson, J. W.; Simner, S. P. Reactivity of lanthanide ferrite SOFC cathodes with YSZ electrolyte. *J. Power Sources* **2004**, *129*, 188–192.
- (58) Yamamura, H.; Nishino, H.; Kakinuma, K.; Nomura, K. Electrical conductivity anomaly around fluorite—pyrochlore phase boundary. *Solid State Ionics* **2003**, *158*, 359–365.
- (59) Seguini, G.; Spiga, S.; Bonera, E.; Fanciulli, M.; Reyes Huamantinco, A.; Först, C.; Ashman, C.; Blöchl, P.; Dimoulas, A.; Mavrou, G. Band alignment at the La₂Hf₂O₇/(001) Si interface. *Appl. Phys. Lett.* **2006**, *88*, 202903.
- (60) Terki, R.; Feraoun, H.; Bertrand, G.; Aourag, H. Full potential linearized augmented plane wave investigations of structural and electronic properties of pyrochlore systems. *J. Appl. Phys.* **2004**, *96*, 6482–6487.
- (61) Qi, Z.; Cheng, X.; Liu, B.; Zhang, G.; Chen, Y.; Li, C.; Yin, M. Vibrational and dielectric properties of $La_2Hf_2O_7$: Experiment and theory. *Solid State Commun.* **2011**, *151*, 1288–1292.
- (62) Gupta, S. K.; Ghosh, P.; Pathak, N.; Tewari, R. Nature of defects in blue light emitting CaZrO₃: spectroscopic and theoretical study. *RSC Adv.* **2015**, *5*, 56526–56533.
- (63) Zhang, K.; Liu, H.-Z.; Wu, Y.-T.; Hu, W.-B. Co-precipitation synthesis and luminescence behavior of Ce-doped yttrium aluminum garnet (YAG: Ce) phosphor: The effect of precipitant. *J. Alloys Compd.* **2008**, 453, 265–270.
- (64) Luwang, M. N.; Ningthoujam, R.; Srivastava, S.; Vatsa, R. Effects of Ce³⁺ codoping and annealing on phase transformation and luminescence of Eu³⁺-doped YPO₄ nanorods: D₂O solvent effect. *J. Am. Chem. Soc.* **2010**, 132, 2759–2768.
- (65) Parchur, A.; Ningthoujam, R. Behaviour of electric and magnetic dipole transitions of $Eu^{3+}, ^5D_0 \rightarrow ^7F_0$ and Eu-O charge transfer band in Li⁺ co-doped YPO₄: Eu^{3+} . *RSC Adv.* **2012**, *2*, 10859–10868
- (66) Soni, A. K.; Joshi, R.; Jangid, K.; Tewari, R.; Ningthoujam, R. S. Low temperature synthesized SrMoO₄:Eu³⁺ nanophosphors functionalized with ethylene glycol: A comparative study of synthesize route, morphology, luminescence and annealing. *Mater. Res. Bull.* **2018**, *103*, 1–12.
- (67) Gupta, S. K.; Reghukumar, C.; Kadam, R. Eu^{3+} local site analysis and emission characteristics of novel $Nd_2Zr_2O_7$: Eu phosphor: insight into the effect of europium concentration on its photoluminescence properties. *RSC Adv.* **2016**, *6*, 53614–53624.
- (68) Singh, L. P.; Srivastava, S. K.; Mishra, R.; Ningthoujam, R. S. Multifunctional hybrid nanomaterials from water dispersible Ca-F₂:Eu³⁺,Mn²⁺ and Fe₃O₄ for luminescence and hyperthermia application. *J. Phys. Chem. C* **2014**, *118*, 18087–18096.
- (69) Gupta, S. K.; Ghosh, P. S.; Yadav, A. K.; Pathak, N.; Arya, A.; Jha, S. N.; Bhattacharyya, D.; Kadam, R. M. Luminescence properties of SrZrO₃/Tb³⁺ perovskite: host-dopant energy-transfer dynamics and local structure of Tb³⁺. *Inorg. Chem.* **2016**, *55* (4), 1728–1740.
- (70) Gupta, S. K.; Sahu, M.; Ghosh, P.; Tyagi, D.; Saxena, M.; Kadam, R. Energy transfer dynamics and luminescence properties of Eu³⁺ in CaMoO₄ and SrMoO₄. *Dalton Trans* **2015**, *44*, 18957–18969.
- (71) Gomes, M. A.; Carvalho, J. C.; Andrade, A. B.; Rezende, M. V.; Macedo, Z. S.; Valerio, M. E. Effects of X-ray irradiation on the $Eu3^+ \rightarrow Eu^{2+}$ conversion in CaAl₂O₄ phosphors. *Opt. Mater.* **2018**, 75, 122–126.

(72) Nag, A.; Kutty, T. The light induced valence change of europium in Sr_2SiO_4 : Eu involving transient crystal structure. *J. Mater. Chem.* **2004**, *14*, 1598–1604.

- (73) Sun, C.; Pratx, G.; Carpenter, C. M.; Liu, H.; Cheng, Z.; Gambhir, S. S.; Xing, L. Synthesis and radioluminescence of PEGylated Eu³⁺-doped nanophosphors as bioimaging probes. *Adv. Mater.* **2011**, 23, H195–H199.
- (74) Werts, M. H. Making sense of lanthanide luminescence. *Sci. Prog.* **2005**, *88*, 101–131.
- (75) Zhang, Y.; Xu, J.; Cui, Q.; Yang, B. Eu³⁺-doped Bi₄Si₃O₁₂ red phosphor for solid state lighting: microwave synthesis, characterization, photoluminescence properties and thermal quenching mechanisms. *Sci. Rep.* **2017**, *7*, 42464.
- (76) Liang, J.; Zhao, S.; Yuan, X.; Li, Z. A novel double perovskite tellurate Eu³⁺-doped Sr₂MgTeO₆ red-emitting phosphor with high thermal stability. *Opt. Laser Technol.* **2018**, *101*, 451–456.